POLITECNICO DI TORINO
Repository ISTITUZIONALE

High-level numerical modeling of complex heating loops with heat pumps and Thermal Energy Storage for energy flexibility analysis

Original
High-level numerical modeling of complex heating loops with heat pumps and Thermal Energy Storage for energy flexibility analysis / Pellizzon, L., Bilardo, M., Fabrizio, E., Perino, M.. - In: APPLIED THERMAL ENGINEERING. - ISSN 1359-4311. - 303:(2026). [10.1016/j.applthermaleng.2026.132261]

Availability:
This version is available at: 11583/3013507 since: 2026-07-24T08:33:07Z

Publisher:
Elsevier

Published
DOI:10.1016/j.applthermaleng.2026.132261

Terms of use:

This article is made available under terms and conditions as specified in the corresponding bibliographic description in the repository

Publisher copyright

(Article begins on next page)

19 November 2026

Applied Thermal Engineering 303 (2026) 132261

Contents lists available at ScienceDirect

Applied Thermal Engineering

journal homepage: www.elsevier.com/locate/ate

Research Paper

High-level numerical modeling of complex heating loops with heat pumps and Thermal Energy Storage for energy flexibility analysis☆

Lorenzo Pellizzon *, Matteo Bilardo, Enrico Fabrizio, Marco Perino

TEBE Research Group, Department of Energy Politecnico di Torino, Corso Duca degli Abruzzi 24, 10129, Torino, Italy

ARTICLE INFO

Keywords:
Heating loop transient modeling
Heat pump
Thermal energy storage
Energy flexibility
Dynamic simulation
TESPy

ABSTRACT

Heat pumps are key to reducing building CO_2 emissions and supporting EU decarbonization goals, but fully exploiting their potential requires integration with Thermal Energy Storage (TES) systems. Accurately analyzing their dynamic behavior and energy flexibility demands high resolution, dedicated dynamic models; by capturing component interactions and transient phenomena during operational transitions, such models can reveal flexibility potentials undetected in steady state simulations. This paper presents an open source Python model integrating water to water heat pumps (WSHPs) with sensible TES. Serving as a preliminary modeling framework, this work lays the foundation for a future digital twin of the HPFlexLab, an experimental facility at the Energy Department (DENERG) of Politecnico di Torino dedicated to advanced building energy management. Results demonstrate the model's ability to reproduce real system behavior across all operating regimes. Validation against an equivalent Modelica model shows that TES temperature profiles exhibit an RMSE below 0.30 °C, a maximum MAE of 0.22 °C, and an MBE up to 0.09 °C; meanwhile, another plant temperature profile of interest yields RMSE, MAE, and MBE values up to 2.19 °C, 0.51 °C, and 0.15 °C, respectively, depending on the operating mode. Furthermore, the Python code is 3 to 9 times faster than Modelica depending on the simulated operating mode and simulation duration. Finally, multiple day energy simulations reveal that the proposed cost minimized control strategy reduces plant operating costs by 5.0% compared to a reference case without TES, despite increasing energy consumption by 10.5% and carbon emissions by 5.7%. Conversely, an emission minimized strategy fails to lower environmental impacts, resulting in an 11.7% increase in electricity consumption and a 1.4% increase in carbon emissions. Consequently, for this case study, TES integration consistently deteriorates both energy consumption and environmental impact compared to the reference configuration.

1. Introduction

One of the greatest challenges facing the energy sector is the energy transition, which encompasses a series of measures aimed at decarbonization through emission reductions [1]. This process is founded on three pillars: lowering energy demand via improved efficiency, shifting to cleaner sources through electrification, and maximizing the integration of variable renewable energy sources (VRES). Achieving these objectives inherently depends on technological advancements, the development of novel materials, and the implementation of advanced control systems [2,3].

The building sector represents a primary target for implementing this transition effectively. It is a highly energy intensive sector, accounting for 26% of total energy consumption in Italy in 2022, primarily driven by heating, cooling, and household appliances [4]. While efficiency technologies such as thermal insulation, heat recovery systems, and natural ventilation are well established and widely applicable to both new and existing buildings [5–7], their widespread deployment is still hindered by economic barriers.

Beyond efficiency, the transition requires deep electrification, especially in space heating. In 2022, IEA data for Italy show that 30.5% of final energy consumption directly relied on natural gas as an energy carrier, predominantly burned in conventional boilers [4]. Displacing this fossil source necessitates substituting traditional boilers with heat pumps, a transition heavily regulated by the Energy Performance of Buildings Directive (EPBD) [8]. Its latest version, approved in May 2024, mandates a progressive phase out of low efficiency boilers and strictly prohibits the installation of new ones after 2040.

The final stage of this framework relies on successfully integrating VRES into the energy mix [9–11]. However, due to the inherent intermittency of renewables, maximizing their utility requires advanced

☆ This article is part of a Special issue entitled: 'SDEWES 2025' published in Applied Thermal Engineering.

* Corresponding author.
E-mail address: lorenzo.pellizzon@polito.it (L. Pellizzon).

https://doi.org/10.1016/j.applthermaleng.2026.132261
Received 12 February 2026; Received in revised form 29 May 2026; Accepted 4 July 2026
Available online 11 July 2026
1359-4311/© 2026 The Authors. Published by Elsevier Ltd. This is an open access article under the CC BY license (http://creativecommons.org/licenses/by/4.0/).

Nomenclature

Acronyms	
COP	Coefficient of Performance
CV	Control Volume
DR	Demand Response
DSM	Demand-Side Management
EPBD	Energy Performance of Buildings Directive
GSHP	Ground-Source Heat Pump
HEX	Heat Exchanger
HP	Heat Pump
HVAC-R	Heating, Ventilation, Air Conditioning and Refrigeration
IEA	International Energy Agency
KPI	Key Performance Indicator
MAE	Mean Absolute Error
MBE	Mean Bias Error
PLR	Partial Load Ratio
RMSE	Root Mean Square Error
SIMPLE	Semi-Implicit Method for Pressure-Linked Equations
SOC	State of Charge
TES	Thermal Energy Storage
VRES	Variable Renewable Energy Sources
WSHP	Water-Source Heat Pump

Symbols	
t	Time [s]
t (vector)	Pump pressure rise vector [Pa]
ρ	Density $[kg/m^3]$
v	Velocity $[m/s]$
τ	Viscous stress tensor [MPa]
L	Length [m]
D	Diameter [m]
D_h	Hydraulic diameter [m]
Ω	Perimeter [m]
S	Cross section $[m^2]$
A	Surface area $[m^2]$
A (matrix)	Incidence matrix [−]
V	Volume $[m^3]$
z	Elevation [m]
p	Static pressure [Pa]
P	Total pressure [Pa]
ϵ	Surface roughness [m]
f	Darcy friction factor [−]
β	Local pressure loss coefficient [−]
G	Mass flow rate $[kg/s]$
M	Mass $[kg]$
M [matrix]	Mass matrix [kg]
T	Temperature [°C]
c_p	Specific heat capacity $[J/kg\ K]$
k	Thermal conductivity $[W/m\ K]$
K (matrix)	Thermal stiffness matrix [W/K]
U	Global heat transfer coefficient $[W/m^2\ K]$
α	Relaxation factor [−]

control strategies and energy storage systems to synchronize generation with demand [12,13]. Furthermore, as high renewable penetration poses risks to grid stability, control strategies must adopt a holistic design capable of incorporating grid requirements [14,15]. Consequently, modern buildings must become both electricity driven and flexible, adapting their load to the needs of the grid, a capability that relies almost entirely on heating and cooling systems. Accurately simulating HVAC-R plant behavior is therefore a fundamental prerequisite; since energy flexibility assessments are strictly dependent on plant simulation, developing detailed and reliable modeling tools is essential to predict performance and validate new control logics. In the following Section 1.1, different modeling approaches found in the literature are reviewed, highlighting their strengths and limitations.

1.1. Literature review

A variety of numerical modeling techniques have been developed in the literature to simulate heating, cooling, and thermal energy storage (TES) systems, providing essential tools to explore the multitude of flexibility strategies required for a successful energy transition. Liu et al. [16] investigated the energy flexibility of different HVAC configurations, demonstrating that the potential to support grid stability through demand response (DR) programs varies significantly depending on whether air conditioning or underfloor heating is deployed. Similarly, Arteconi et al. [17] implemented demand-side management (DSM) strategies for a domestic heating system comprising a heat pump, a TES unit, and two different distribution networks, namely radiators and underfloor heating. Both studies reinforce the premise that unlocking the full flexibility of thermal systems requires robust, dynamic models capable of faithfully representing complex interactions, such as TES charging cycles and setpoint modulations, which steady-state or quasi-steady-state analyses typically overlook.

To establish a systematic framework for these modeling choices, Afram et al. [18] reviewed the literature on HVAC systems to categorize the available modeling methodologies into black, gray, and white box approaches. Although recent trends in artificial intelligence have driven increasing interest in data driven analysis and black box formulations, developing accurate empirical models demands large amounts of historical data. Such data are often unavailable in practice, particularly when the energy plant has yet to be constructed. Consequently, to overcome potential data scarcity while ensuring high physical fidelity, the current work focuses on white box modeling.

A significant body of literature uses white box models to conduct flexibility analyses, frequently relying on established commercial tools such as TRNSYS and Modelica, either directly for system simulation or as a baseline for validation. For instance, Wang et al. [19] investigated the feasibility of retrofitting a chiller-gas boiler system with a ground-source heat pump operating in both cooling and heating modes, using TRNSYS to conduct energy performance simulations on an hourly basis. Following a similar methodological approach, Coccia et al. [20] analyzed an integrated HVAC, refrigeration, and water loop heat pump system in a supermarket by developing a TRNSYS model integrated with external manufacturer performance curves, utilizing a 5 min time step to test predictive rule based control strategies under real-time pricing.

In parallel, the equation based language Modelica, executed within the Dymola environment, has emerged as a powerful tool for district and building scale flexibility assessments. Guo et al. [21] used hourly Modelica simulations to evaluate a novel bidirectional thermal substation incorporating thermal energy storage and a space heating heat pump within a fifth-generation district network, proving that such models successfully optimize network interaction. At the building level, Tian et al. [22] developed a physical lumped parameter RC equivalent circuit model validated in Modelica to reproduce the multizone thermal dynamics of an air conditioning system. Discretizing the dynamic thermal equations with a 5 min time step enabled a convex optimization framework to map the flexible power of the HVAC system in real time. Extending this toolset to the industrial sector, Vogt et al. [23] analyzed the energy flexibility of an HVAC system serving a lithium-ion battery cell manufacturing dry room. Due to strict hygrothermal requirements, the authors developed a validated Modelica model of the air conditioning plant and controlled volumes, generating physical simulation data at a 15 min output interval while evaluating predictive rule based control strategies via an hourly check.

1.2. Aim of the work

The literature review reveals that the majority of research in the field of energy simulation and flexibility analysis predominantly relies on commercial software, such as TRNSYS and Modelica based environments (e.g., Dymola), often utilizing larger time steps. Consequently, these approaches might overlook certain fast transient behaviors that could be fundamental for flexibility analysis, potentially limiting the ability to fully evaluate and exploit the system flexibility potential. Therefore, a distinct gap remains for a robust, open source numerical model capable of operating with reduced simulation time steps at a low computational cost to conduct detailed simulations of HVAC systems integrated with heat pumps and TES, as proposed in this study. To this end, a different methodology is introduced for modeling the HVAC hydraulic network, based on the Semi-Implicit Method for Pressure-Linked Equations (SIMPLE) algorithm [24]. While traditionally employed to solve complex fluid dynamics problems, this approach is adapted here to handle a 1D hydraulic network. This mathematical formulation proves to be highly efficient and computationally fast, successfully overcoming the overhead of simultaneous equation solvers.

This research is conducted within the framework of the HpFlexLab project, an experimental facility currently under development at the Energy Department (DENERG) of the Politecnico di Torino. Designed to test and optimize innovative building energy management solutions, the laboratory plant features a symmetrical configuration consisting of two separate thermal loops: a hot circuit and a cold circuit. Both loops are equipped with their own TES and thermal load, and the entire system is powered by two parallel Water Source Heat Pumps (WSHPs). The ultimate goal of the broader project is to develop a comprehensive digital twin of this facility to enable real time simulations and validate advanced control logics capable of enhancing system flexibility. Consequently, this infrastructure will support the investigation of active management strategies, such as load shifting and demand-side management, under dynamic pricing scenarios and fluctuating renewable energy contributions.

Within the context of this extensive initiative, the present work focuses specifically on the hot side of the system. The primary objective is to develop an open source Python tool capable of accurately modeling the transient operations of the flexible heating loop with heat pumps and storage units. As the physical laboratory is currently under construction and experimental data are not yet available, the proposed numerical model is validated against an equivalent high fidelity model developed in the Modelica environment. Once validated, the Python tool is applied to a specific case study to conduct detailed energy flexibility analyses. Through this approach, this study serves as a foundational step, integrating a preliminary modeling framework into a full digital twin for the HPFlexLab experimental facility.

2. Methodology

This section is divided into three main parts, starting with a description of the modeling approach adopted in this work, followed by an analysis of the operating modes of the analyzed heating systems, and concluding with the validation methodology for the developed model.

2.1. Heating systems modeling

Heating systems typically consist of complex hydraulic networks, frequently in looped configurations, interacting with active components like circulation pumps, valves, boilers, heat pumps, thermal loads, heat exchangers, and thermal storage units. Accurate simulation requires a modular approach where each component is modeled and dynamically coupled to capture the true operational behavior of the system.

Based on this modular requirement, this section details the modeling approaches used to describe the main components, including the heat pump, thermal load, TES, and hydraulic network, as well as the integration of these individual models to simulate the entire system. It should be noted that the description provided in the following subsections focuses on the modeling approach, without reference to specific software. While specific tools were employed in this work (see Section 3), the methodology is generalizable; any tool capable of deriving equivalent parameters and results may be adopted.

2.1.1. Heat pump model

The heat pump employed in this work is a variable-speed water source heat pump (WSHP); its modeling is essential to characterize the machine's performance under the specific operating conditions it is required to maintain.

In particular, the model accepts as inputs the water inlet temperatures and flow rates at both the condenser and evaporator. Additionally, it requires the supply temperature set-point, which corresponds to the target outlet temperature at the condenser (in heating mode) or the evaporator (in cooling mode). The model outputs the COP and the provided thermal capacity, which are used to evaluate the overall energy consumption of the system.

Based on the previous discussion (see Section 1.1), a white-box modeling approach has been chosen for the heat pump. Consequently, this necessitates a physics-based method involving the modeling of each individual component (i.e., compressor, condenser, evaporator, and expansion valve).

2.1.2. Thermal load model

The user's required thermal load is defined as a known, time-dependent thermal power profile. It is modeled using a single heat exchanger (HEX), where technical water transfers energy to the fluid circulating in the user's distribution system.

On the user side, supply and return temperatures are maintained constant, while the exchanged thermal power varies with the flow rate. Consequently, the model calculates the outlet temperature based on the technical water's inlet flow rate and temperature by solving the energy balance equation.

2.1.3. Thermal energy storage model

The thermal energy storage (TES) consists of a sensible water tank with an internal copper serpentine coil designed to exchange heat with the circulating technical water. The tank is modeled as a fully mixed volume due to the presence of stirrers; these increase the fluid velocity, thereby enhancing the heat transfer coefficient between the stored water and the serpentine.

The model solves the transient energy balance equations for the tank fluid and the fluid flowing through the serpentine. Given the inlet flow rate and temperature of the technical water, the model dynamically calculates the serpentine outlet and tank temperatures.

Further details regarding the TES constitutive equations are provided in Appendix A.2.

2.1.4. Hydraulic network model

The hydraulic network is the subsystem responsible for transferring energy among the heating system's components. Modeling such a network requires calculating pressure, flow rate, and temperature distributions to accurately represent the system's state.

In Fig. 1, a scheme representing the methodology workflow is shown. The first step consists of deriving the Navier–Stokes equations (mass and momentum conservation equations) along with the energy conservation equation for the constitutive elements of a network (branches and nodes). Since HVAC pipes typically have length to diameter ratios in the tens or even hundreds, the modeling goal shifts from describing the distribution of temperature, pressure, and flow rate across the pipe cross section to determining these values at the main nodes and branches. This makes the 1D assumption highly effective and

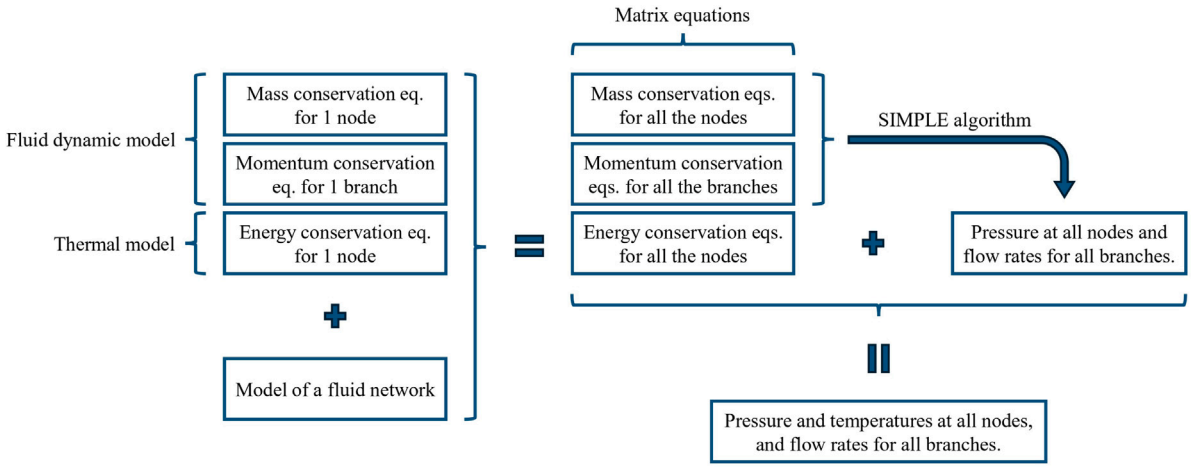


Fig. 1. Methodology workflow.

not at all restrictive, allowing the governing equations to be reduced to a single dimension.

To solve the problem, these equations must be applied to all elements of the network, meaning that an effective modeling of the network is required, which can be achieved by applying graph theory [25]. Then, by combining this model with the previously derived 1-D equations, a set of equations describing the fluid dynamics and thermal problem for the entire network can be easily derived. These equations can then be grouped together in matrix form.

At this point, the matrix equation must be solved. First, the fluid dynamic problem is addressed, using the SIMPLE algorithm, which is suitable for efficiently solving large networks typically found in district heating applications [26]. Once the pressure and flow rate distributions in the network are known, the thermal problem can be addressed, also deriving the temperature distribution in the network.

Further details regarding network modeling, the derivation of the thermo-fluid dynamic equations for this application, and their solution using the SIMPLE method can be found in Appendix A.1 or more specifically in the book by Sciacovelli et al. [27].

2.1.5. Solving procedure

The final step of the simulation involves integrating the component models with the network model. These components are essential for computing specific boundary conditions required to solve the network, thereby determining pressures, temperatures, and flow rates throughout the nodes and branches under various operating conditions.

Fig. 2 schematically represents the overall solution procedure. Certain aspects of the flowchart, particularly the initial steps concerning the pump pressure gain computation, will be detailed in Section 3.1.1. Assuming the pump pressure gain is correctly defined to ensure the target flow rate for a specific operation, it serves as the primary boundary condition for the SIMPLE algorithm. This algorithm computes nodal pressures and branch flow rates with a time step of 1 min; during this interval, the pressure gain BC is held fixed, and consequently, the hydraulic variables are determined.

Subsequently, using the computed flow rates and the nodal temperatures from the previous time step, the component models are solved. This enables the computation of specific thermal boundary conditions (temperatures at specific nodes), allowing the thermal problem to be solved with a finer time step of 1 s to define the temperatures at all nodes.

Regarding time discretization, once the SIMPLE algorithm is solved, the hydraulic variables (pressure and flow rates) are considered constant for the duration of the 1-minute time step. Within this interval, the thermal problem is solved with a finer resolution of 1 s (i.e., 60 iterations per hydraulic step). This iterative process, where fluid dynamics are updated every minute and the thermal state every second, continues until the end of the simulation time.

The choice of using two different time steps is further detailed in Section 3.1.1.

2.2. Heating system operating modes

The plant was designed for maximum flexibility, allowing it to switch between multiple operating modes and strategies. Fig. 3 shows a functional diagram of the plant, highlighting its main components (HP, TES, and thermal load).

Specifically, the operating modes are:

- **Preheating:** the water flow bypasses the TES and the thermal load, recirculating through the HP, which operates at constant power (half of the nominal capacity) and flow rate. This mode is activated when the plant is cold; before supplying the load or charging the TES, the water must be preheated to reach a usable temperature level.
- **Energy charging:** the flow is directed through the TES to heat the stored water until the SOC reaches 1. The HP supplies water at a constant temperature and flow rate.
- **Direct heating:** the HP directly supplies hot water to the user at a constant temperature. The flow rate is variable, depending on the required thermal load.
- **Energy discharging:** the HP is off, and the TES provides the thermal power required by the user. The flow rate varies according to the thermal load, and the process continues as long as the SOC is greater than 0, meaning the TES temperature stays above a minimum threshold.

In practice, the plant could be operated in additional modes. However, as a starting point for the modeling, just these four have been considered.

2.3. Heating system model validation

The model developed in this work is validated by building an equivalent version in the Modelica language, specifically within the OpenModelica environment, and comparing the simulation results of both. Modelica was chosen because it is widely used and well established for HVAC system simulations. The validation model was constructed using standard components from the Modelica Standard Library (MSL) and the Buildings Library [28].

The two models are compared across simulations of the three main operating modes: direct heating, energy charging, and discharging.

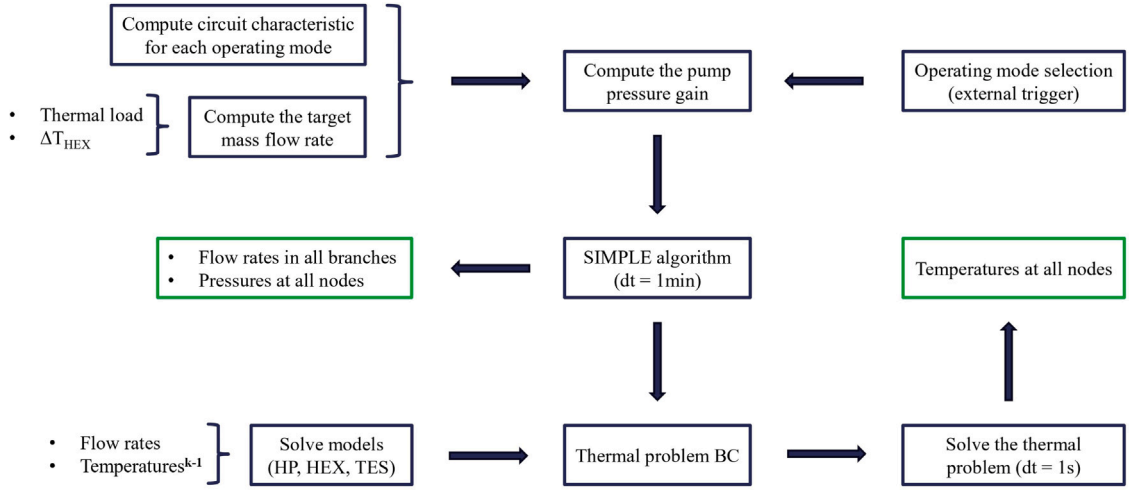


Fig. 2. Flowchart of the overall solution procedure.

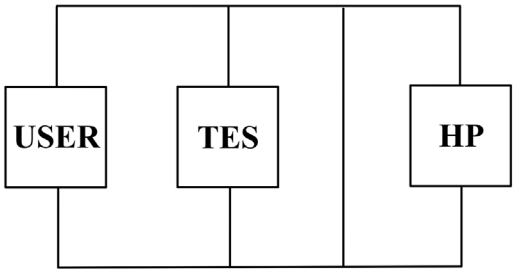


Fig. 3. Functional diagram of the heating system.

Specifically, the temperature profiles upstream of the thermal load are compared during the direct heating and discharging phases. For the charging phase, the temperature profile of the TES is evaluated over a sequence of charging and discharging cycles, separated by periods when the system is inactive (rest mode).

To quantify the discrepancy between the temperature profiles simulated in Modelica (taken as the reference) and those from the developed model, three metrics are calculated: root mean square error (RMSE), mean absolute error (MAE), and mean bias error (MBE). Additionally, the computation times are compared to evaluate the computational cost of both models (they operate with the same time step).

3. Case study

3.1. Plant description

The heating plant under analysis is an experimental facility to be built at the Politecnico di Torino. Although the plant is not yet operational and its exact geometric and constructive details are not fully finalized, the necessary parameters for the simulations have already been defined. Specifically, the pipe lengths, diameters, insulation thicknesses, insulation materials, and valve pressure loss coefficients have been defined based on the system design to conduct the simulations.

Fig. 4 shows the network topology of the heating system, which consists of 17 branches (branches b_{12} and b_{13} are not included in the count) and 14 nodes. The valves located on the branches allow for continuous control by varying their cross-section from fully open to closed. This regulation permits changing the operating mode of the system, as discussed in Section 2.2.

Branches b_3 and b_4 feature two identical water-to-water heat pumps. Specifically, each branch represents the heat exchanger side where the technical water flows, absorbing heat from the heat pump condenser. Similarly, branch b_9 represents the technical water side of the heat exchanger (HEX) connected to the external load, where the water releases thermal energy to the user. The two pink rectangles represent identical TES tanks connected in parallel. Each tank contains a copper serpentine coil where the system water flows to exchange heat with the water stored inside the tank. These coils are not included in the network model.

To simulate the complete system shown in Fig. 4, both the hydraulic network and its main components must be modeled. While Section 2 outlines the general methodology, this section provides the plant specifications and further modeling details. Specifically, the network and TES models were developed directly in Python by translating the mathematical methods into numerical code. Conversely, the HP and HEX components are simulated using the Thermal Engineering Systems in Python (TESPy) library [29], an open-source tool for steady-state simulations of energy systems.

The following subsections describe each component and its implementation in detail.

3.1.1. Hydraulic network specifications

Table 1 lists the main geometric characteristics of the hydraulic network modeled in Python, along with the initial and boundary conditions. These conditions are used to solve the fluid-dynamic problem, which defines the pressure and flow rate distributions in the network through the SIMPLE algorithm (see Section 2.1.4).

As regard the fluid-dynamic problem, from a plant control perspective, the primary target to impose on the system is the circulating mass flow rate. During the preheating and energy charging phases, this mass flow rate is set by the user to a fixed value. Conversely, during the direct heating and energy discharging phases, the mass flow rate varies according to the thermal power required by the load, which is enabled by operating the circulating pump at variable speed. By imposing a temperature drop across the HEX of $\Delta T_{HEX} = 5°C$ and knowing the supplied thermal power, the target mass flow rate can be readily calculated.

However, within the SIMPLE algorithm, it is not possible to impose the mass flow rate directly as a boundary condition; instead, the fluid dynamics problem requires boundary conditions expressed in terms of pressure. Regarding these boundary conditions, the total pressure is fixed at a single node in the circuit, specifically node 14, downstream of the circulating pump, to establish a reference pressure value for the network. The critical boundary condition to define, however, is the pump pressure gain, which directly governs the circulating mass flow rate.

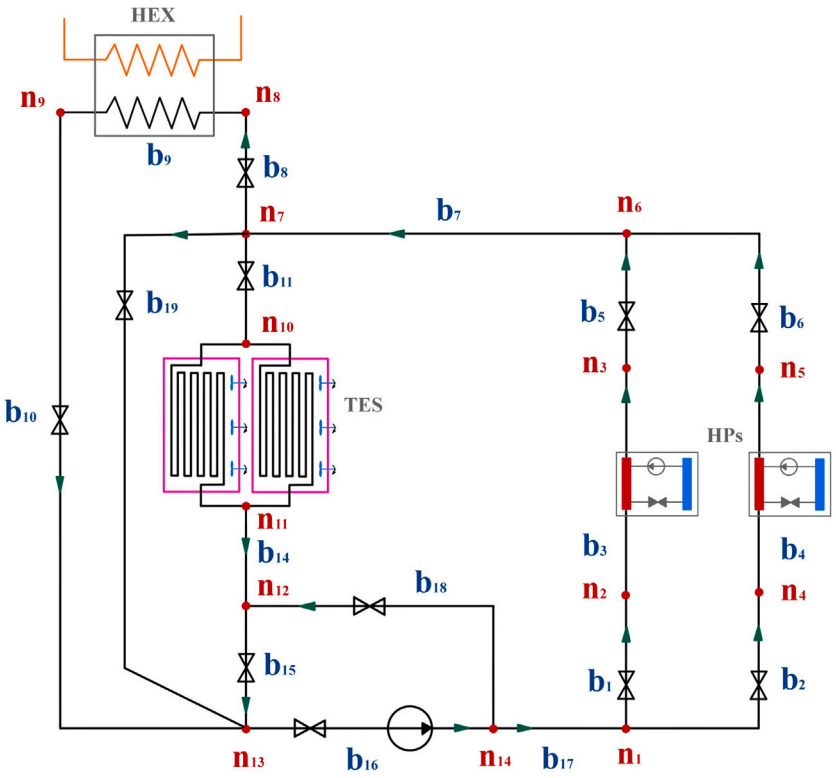


Fig. 4. Schematic representation of the heating system (not in scale).

Table 1
Hydraulic network specifications, numerical settings and initial and boundary condition for the fluid-dynamic problem.

Specification	
Number of branches	17
Number of nodes	14
Pipe inner diameter[a]	0.035 m
Pipe length	4 m
Pipe insulation thickness	0.020 m
Pipe roughness (ϵ)	15e−7 m
Insulation thermal conductivity	0.03 $\frac{W}{mK}$
Valve's loss coefficient (β_j)	3
Numerical settings	
Time-step (fluid dynamic problem)	1 min
Time-step (thermal problem)	1 s
Fluid dynamic boundary conditions (for all the operating modes)	
Total pressure at node n_{14}	200 000 Pa
Target flow rate (in preheating and energy charging)	Input (1.8 m^3/h)
Target flow rate (energy charging)	Input (2.9 m^3/h)
Fluid dynamic initial conditions	
Total pressure across all nodes	100 000 Pa
Pump pressure gain	0 Pa

[a] The inner diameter indicated in the table applies to all branches except for b_1, b_2, b_3, b_4, b_5 and b_6 whose inner diameters are 0.025 m.

To bridge this gap and achieve the target flow rate, the relationship between pressure gain and flow rate must be established for each network configuration across the various operating modes. This is achieved by simulating a parameter sweep of the pump pressure gain for each circuit configuration to define the characteristic curve relating pressure gain to mass flow rate. From this curve, the pump pressure gain required to achieve a specific target flow rate can be determined and imposed in the simulation.

Finally, the fluid dynamic problem is solved under steady conditions because the transient duration depends on the propagation speed of pressure waves in water. Since this speed is extremely high, the resulting transient is so rapid that it can be safely considered negligible.

Although the problem is solved under steady conditions, any variation in the boundary conditions alters the distribution of pressures and flow rates. Since the thermal load profile (see Section 3.2) is discretized using a 1 min time step, and given that the load determines the mass flow rate and consequently the pump pressure gain, the time step for the fluid dynamics problem is likewise set to 1 min.

The thermal problem is solved once the fluid dynamics are defined, meaning the flow rate distribution is already known. For this analysis, a small time step is necessary to capture the phenomenon because the thermal transient evolves at the speed of the water in the pipe, which reaches a maximum of 1 m/s. Specifically, the time step value of 1 s was determined through a sensitivity analysis conducted during the validation process. By progressively decreasing the time step, the error metrics reached an asymptote at that specific value, ensuring that further reductions would not significantly improve accuracy. Consequently, while a new pump pressure gain is updated every 60 s, the transient thermal model is solved at each 1 s interval, using the conditions from the previous second as the starting point. Finally, the boundary conditions required to solve the thermal problem are derived from the component models described in the following subsections. Specifically, these conditions consist of temperature values imposed at specific nodes of the network, which enables the solution of the thermal equations.

3.1.2. Thermal energy storage specifications

Table 2 summarizes the main geometric characteristics of each storage unit, including details regarding their operating conditions. The TES constitutive equations are implemented directly in Python (see Appendix A.2). Within the context of the thermal problem, the model is used to calculate the time evolution of both the TES temperature and the water outlet temperature from the internal coil. Once this outlet temperature is calculated, it is imposed as a boundary condition for the network thermal problem, specifically setting the temperature at node 11 or node 10, depending on the operating mode (TES charging or discharging).

Table 2
TES specifications and operating conditions.

Specification	
TES water mass	2450 kg
TES dimensions ($L \times \phi$ - cylindrical shape)	2 × 1.25 m
Insulation thermal conductivity	0.03 $\frac{W}{mK}$
TES insulation thickness	0.030 m
TES operating conditions	
Maximum TES temperature ($T_{TES,max}$)	55°C
Minimum TES temperature ($T_{TES,min}$)	45°C

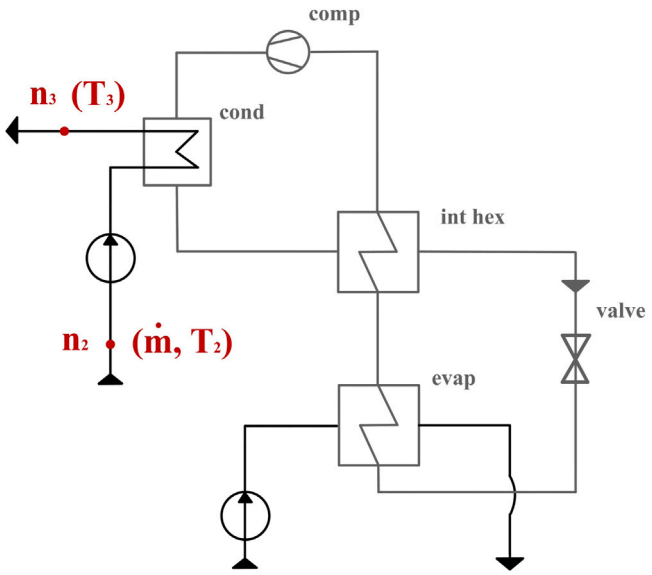


Fig. 5. Scheme of the HP implemented in TESPy.

3.1.3. Heat pump specifications

Fig. 5 presents the schematic of the heat pump simulated in TESPy. It is a variable-speed, water-to-water unit that uses R410a as the refrigerant and operates on a simple single-stage vapor compression cycle with a rated heating capacity of 10 kW. An internal heat exchanger ensures the superheating of saturated vapor from the evaporator while simultaneously subcooling the saturated liquid from the condenser. While constant pressure drops and efficiencies are assumed for all heat exchangers, a variable isentropic efficiency is considered for the compressor, which varies based on the partial load ratio.

On the evaporator side, the technical water has a constant flow rate and inlet temperature, which are not relevant to this research since the focus is on the hot side of the system. Conversely, on the condenser side, the inlet water flow rate and temperature are defined by the values computed at the previous time step from the network thermal problem solution at nodes n_2 and n_4 (see Fig. 4). The supply temperature or the heating capacity is imposed on the HP model based on the operating mode, such as direct heating, energy charging, or discharging (see Table 3). The model then computes the remaining variable (heating capacity or supply temperature), along with the refrigerant flow rate and the resulting COP. Regarding the thermal problem, the HP supply temperature is used as a boundary condition at nodes n_3 and n_5, whether it is directly imposed or computed by the model.

Fig. 6 illustrates the performance map of the HP modeled in TESPy as a function of the hot water supply temperature and the partial load factor, defined as the ratio of the actual capacity to the nominal capacity of the machine. All parameters regarding the source side of the HP, the cold one, are kept constant. As expected, the COP increases as the supply temperature decreases.

Table 3
HP specifications and operating conditions.

Specification	
HP rated thermal capacity	10 000 W
Refrigerant	R410a
HP operating conditions	
HP thermal capacity (preheating)	5000 W
HP supply temperature (energy charging)	60°C
HP supply temperature (direct heating)	50°C

3.1.4. Thermal load specifications

Fig. 7 illustrates the schematic of the heat exchanger representing the thermal load. Like the HP model, this component is implemented in TESPy and operates under steady conditions. The gray pipes represent the secondary circuit, where an ideal power absorption equal to the thermal load and the temperatures across the heat exchanger are imposed, while the flow rate varies accordingly. Conversely, the black pipe represents branch b_9 (see Fig. 4) of the primary circuit. Using the inlet flow rate and temperature from the previous time step obtained from the network thermal model solution, this model computes the outlet temperature at node n_9. This temperature is then fed back to the network as a thermal boundary condition.

The minimum temperature to be maintained at node n_8 to supply thermal power is set to $T_{8,min} = 40$°C.

3.2. Thermal load

Once the development of the model has been detailed and its validation completed (see Section 2.3), it can be used to perform energy simulations. Specifically, in the case study analyzed in this work, the energy consumption, operating costs, and carbon emissions of the plant are computed over a three day period. Different control strategies are then tested to assess the plant's flexibility potential in reducing either operating costs or carbon emissions.

To carry out the simulation, the thermal load profile must first be defined, which remains identical across all the adopted strategies. Fig. 8 describes its trend over the three day simulation window. The load profile is discretized on a one minute basis, repeating identically each day with an active window from 7:00 to 20:00 and a peak power of 19 500 W. This profile has been defined based on the average energy needs of the various experimental facilities within the university laboratory where the plant will be installed [30].

3.3. Energy simulation boundary conditions

As illustrated in the previous subsection, the flexibility analysis relies on evaluating the plant's operating costs and carbon emissions. Consequently, both the electricity price and carbon intensity profiles must be defined for the simulation window. Specifically, Fig. 9 shows the trend of these two profiles from October 15 to 17, 2024, focusing on the Northern Italy bidding zone. This specific period was selected due to data availability.

The electricity prices were retrieved from the official database of the Italian electricity market operator [31], while the carbon intensity data were sourced from Electricity Maps [32]. Both datasets are discretized on a fifteen minute basis.

3.4. Plant control strategies

Considering the plant architecture (see Fig. 4), TES units represent the primary source of flexibility. These systems allow electricity consumption to be shifted over time, decoupling it from the thermal load curve. Consequently, they can prevent HPs from operating during periods of high electricity costs or high carbon intensity.

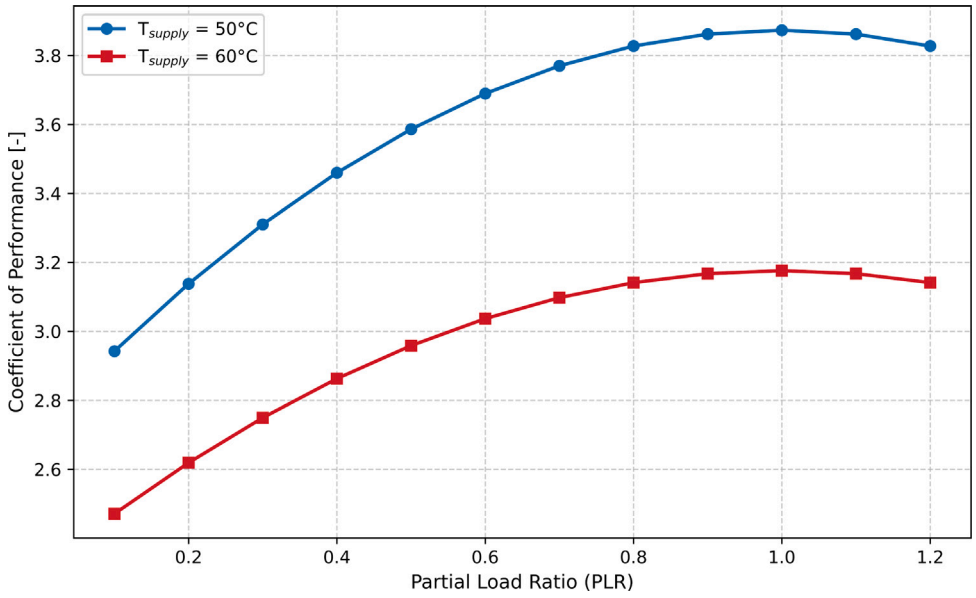


Fig. 6. HP performance map as a function of the supply temperature and partial load ratio (PLR).

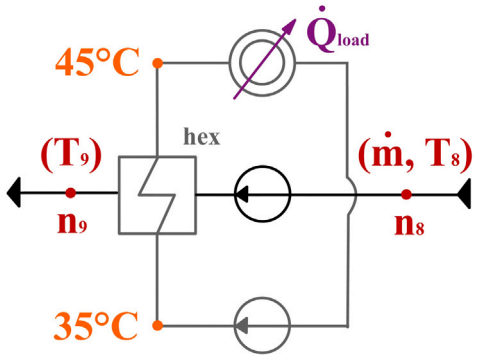


Fig. 7. Scheme of the HEX implemented in TESPy.

However, thermal storage also introduces certain drawbacks. While their capital cost is excluded from this analysis, their energetic penalties are fully considered. First, storage units introduce thermal losses, which inherently increase overall energy consumption. Second, as discussed in Section 3.1.3, charging the storage requires a higher supply temperature from the HP compared to direct heating. This temperature increase degrades the efficiency of the machine (see Fig. 6), leading to higher electricity consumption.

Therefore, the net benefit of using thermal storage is not obvious a priori. To evaluate this trade-off, this case study compares three scenarios with identical thermal loads but different control strategies. The baseline scenario relies entirely on direct heating, meaning the heat pumps feed the user thermal load directly, as if the storage were absent. In contrast, the second and third scenarios utilize the storage, managing its operation to minimize either the operational costs or the carbon emissions of the system.

3.4.1. Cost or emissions minimization strategy

The cost or emissions minimization strategy is based on a simple algorithm. Given the cost or emissions profile and the thermal load curve for the simulated period (see Figs. 8 and 9), the algorithm determines the optimal schedule to charge and discharge the thermal storage.

Specifically, the charging period is restricted to the timeframe from 20:00 to 07:00 the following day, when there is no thermal load. Since the cost and emissions curves are discretized every fifteen minutes, this potential charging window is divided into quarter-hour intervals. These intervals are then sorted in ascending order, from the lowest to the highest cost or emissions. Based on the maximum energy capacity of the tank and the average thermal flux between the coils and the storage, the time required to fully charge the system is known. The best quarter-hour intervals (those with the lowest cost or emissions) are then selected for the charging process.

The discharging process follows a similar logic. Given the period with thermal load demand (from 07:00 to 20:00) and the energy available in the storage, the quarter-hour intervals are sorted in descending order, from the highest to the lowest cost or emissions. Based on the available energy, the algorithm selects the best intervals to discharge the storage (those with the highest cost or emissions). During the remaining hours, the heat pumps operate in direct heating mode. Consequently, at the end of the load demand period, the state of charge (SOC) of the storage reaches 0, which corresponds to a temperature of 45°C.

The initial TES temperature is set to 44.5°C because it typically drops by 0.5°C between the end of the discharging phase and the start of the next charging cycle.

3.4.2. The flexibility factor

Following the simulation of the different control scenarios, a comparative analysis is performed to evaluate the energy flexibility of the system. The literature offers various metrics for quantifying the energy flexibility of buildings and HVAC systems, which have been thoroughly reviewed in the IEA EBC Annex 67 Energy Flexible Buildings report [33]. Among the KPIs discussed in the literature, the flexibility factor defined by Le Dréau and Heiselberg [34] is selected and calculated using the following equation:

$$\text{Flexibility factor} = \frac{\int_{\text{fav}} \dot{q}_{\text{heating}} dt - \int_{\text{unfav}} \dot{q}_{\text{heating}} dt}{\int_{\text{fav}} \dot{q}_{\text{heating}} dt + \int_{\text{unfav}} \dot{q}_{\text{heating}} dt} \quad (1)$$

The numerator of the flexibility factor represents the difference between the energy consumed during favorable and unfavorable periods. The denominator, instead, consists of the sum of these two terms, representing the total energy consumption. The definition of a "favorable" period depends on the specific objective of the analysis. In this study, favorable and unfavorable time windows are defined based on two variables: energy cost and carbon intensity.

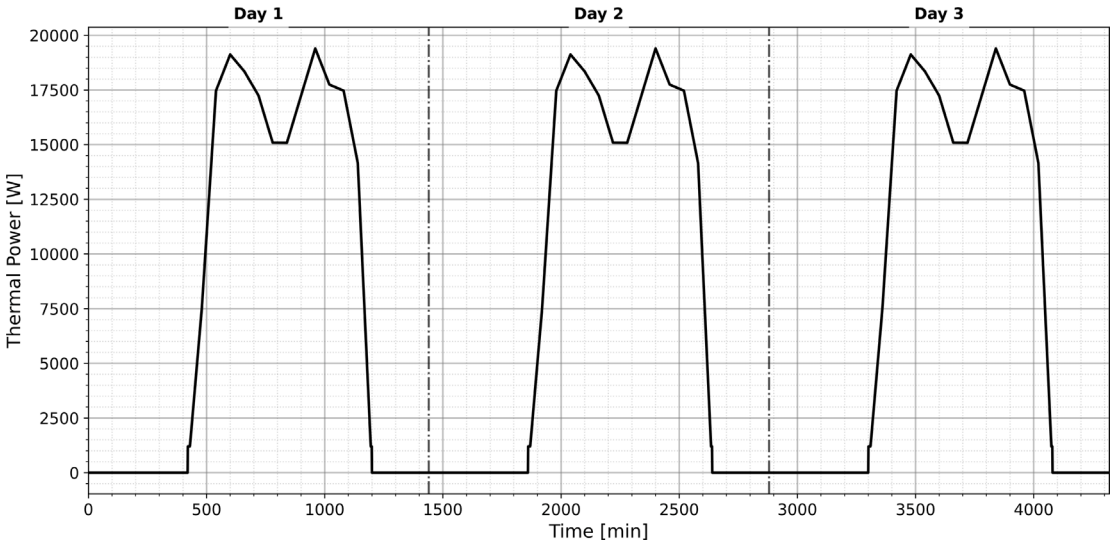


Fig. 8. Thermal load curve on a minute basis [30].

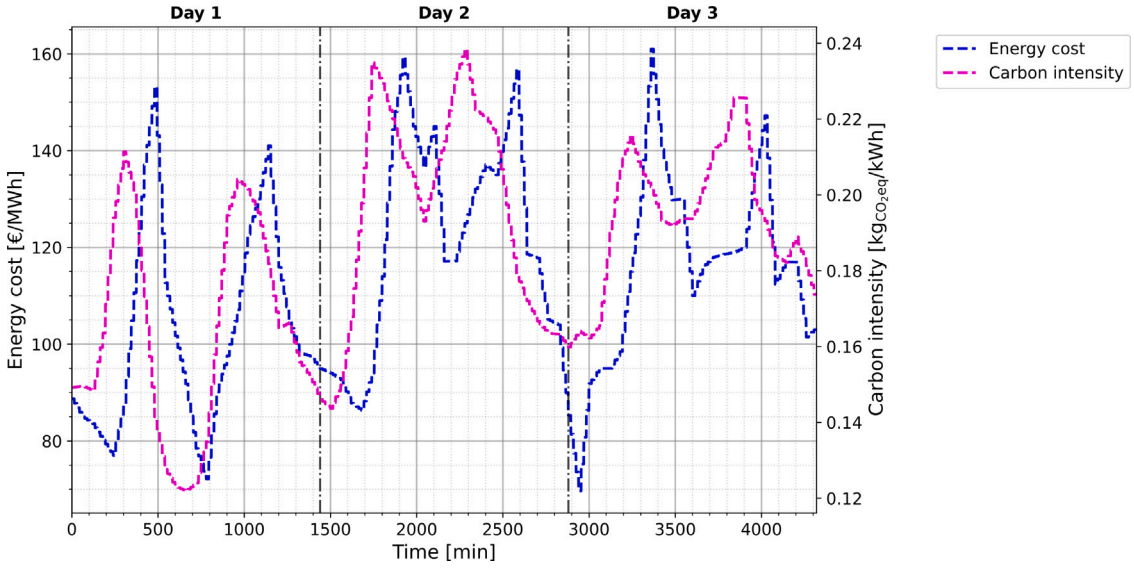


Fig. 9. Energy cost and carbon intensity profiles for the simulated period [31,32].

By definition, this factor ranges from −1 to +1. A value of −1 indicates a rigid, non-flexible system that is unable to shift its consumption to favorable periods. Conversely, a value of 1 represents a highly flexible system, capable of fully displacing its energy demand to coincide with favorable time intervals.

The definition of favorable and unfavorable periods is essentially arbitrary. In this work, the distribution of electricity cost and carbon intensity was divided into quartiles: a favorable period is defined as any time interval falling within the first quartile, while an unfavorable period corresponds to the fourth quartile.

4. Results

This section is divided into two parts. The first part focuses on the validation of the numerical model developed in Python through a comparison with the Modelica model. The second part presents an energy flexibility analysis performed using the Python model.

4.1. Model validation

The numerical model validation is performed by comparing the temperature profiles simulated in Python with those simulated in Modelica, focusing on specific plant nodes and elements under distinct operating modes.

Fig. 10 illustrates the temperature evolution at the thermal user upstream node (n_8) during direct heating mode for both Python and Modelica models. In this mode, the heat pump directly supplies the load to meet the thermal demand. Initially, the temperature is 15°C as the system is off and cold; once demand arises, the heat pumps deliver flow at the required setpoint of 50°C. A notable difference is the oscillation observed in the Modelica simulation, which is absent in the Python model. This discrepancy stems from the control logic: Modelica utilizes a PI controller to regulate the supply temperature, whereas Python treats the supply temperature as a boundary condition, maintaining it constant as soon as demand occurs. Furthermore, the Python model temperature slightly exceeds 50°C due to a preheating phase prior to direct heating, which raises the water temperature to

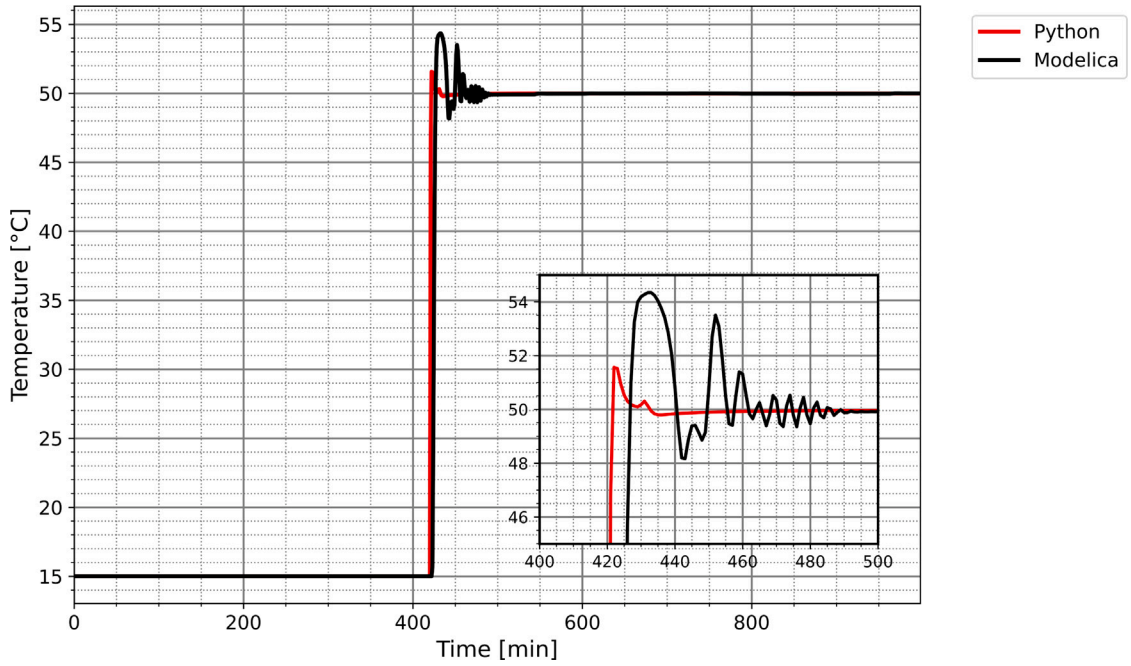


Fig. 10. Simulated temperature profiles at the upstream node of the thermal user (n_8) during direct heating mode.

55°C. Consequently, when the operating mode changes, the initial hot water front reaching node n_8 is above the 50°C setpoint.

Using the Modelica results as a reference, the Python model achieves an RMSE of 2.19°C, a MAE of 0.24°C, and an MBE of 0.10°C. In terms of computational cost, the Modelica simulation requires 615 s, while the Python model completes in 184 s.

Fig. 11 illustrates the temperature evolution at the thermal user upstream node and the TES temperature during a discharging phase, comparing the Python and Modelica models. Initially, the system operates in charging mode, with the TES temperature increasing until minute 20, when the thermal load requires power and the system switches to discharging mode. As previously noted, the sections of the plant not involved in charging remain idle and cold. When the operating mode changes, the water within the TES coils is directed toward the thermal load, causing a temperature rise at node n_8. In both models, this temperature exceeds the bulk TES value because the initial front reaching the user was heated to 60°C during the charging phase.

Using the Modelica results as a reference, error metrics were calculated. For the user temperature (T_{user}), the RMSE is 1.29°C, the MAE is 0.51°C, and the MBE is −0.15°C. Regarding the TES temperature, the model achieves an RMSE of 0.046°C, a MAE of 0.043°C, and an MBE of 0.038°C. In terms of computational cost, the Modelica simulation requires 124 s, while the Python model completes in 41 s.

Fig. 12 shows the TES temperature profile over a day. The system operates in various modes, selected in an arbitrary sequence to evaluate the TES response in each case. At the start of the simulation, the SOC is 0 as the temperature is near 45°C. A charging phase follows, bringing the storage to approximately 55°C, which corresponds to SOC = 1. Subsequently, rest and discharging modes alternate (identifiable by the different slopes in the temperature profile) until the storage is fully discharged, returning to 45°C. The sequence of operating modes follows the same schedule in both models, and the boundary conditions for both simulations are identical.

Using the Modelica results as a reference, the error metrics are calculated as follows: RMSE is 0.30°C, MAE is 0.22°C, and MBE is 0.09°C. Regarding computational cost, the Modelica simulation requires 1853 s, while the Python simulation takes 200 s.

4.2. Energy simulations

Once the python model is validated, it is used to analyze the case study described in Section 3.2. The main results regarding temperature profiles and other key variables are reported below to compare the different simulated scenarios.

Fig. 13 illustrates the TES temperature profile and electricity cost over the three-day simulation period, under a cost-minimized operating schedule. The colored areas represent the plant operating modes, while the absence of shading indicates the rest mode. Since storage charging is restricted to nighttime, the charging phases occur when electricity costs are at their lowest. Similarly, the alternating use of discharging and direct heating to meet the daytime thermal load is managed by prioritizing the storage when energy costs are higher, while the heat pumps operate in direct heating mode during periods of minimum cost.

Fig. 14 mirrors Fig. 13 but replaces energy cost with carbon intensity, reflecting an emission-minimized operating schedule. The timing and logic for switching between modes remain consistent with the previous case, though carbon intensity now serves as the primary driver for mode selection.

Fig. 15 compares the TES temperature profiles for the cost and emission minimization schedules. Because energy cost and carbon intensity follow similar trends during nighttime, the charging phases in both scenarios are largely overlapping. Significant differences emerge during daytime hours, resulting in distinct storage discharge schedules.

Table 4 reports the total electricity consumption of the system (heat pumps and circulation pumps), along with the resulting costs and CO2 emissions, based on the three-day energy simulation. These results are calculated for both the cost-minimized and emission-minimized scenarios, as well as for a direct heating reference case. In the reference scenario, storage is not used and the thermal load is met directly by the heat pumps as required.

Fig. 16 presents three charts comparing the performance of the various operating schedules based on the metrics in Table 4. As expected, the two solutions using thermal energy storage (TES) lead to an increase in electricity consumption. This is due to thermal losses from the storage and the fact that during charging phases, the heat pump supply temperature is 60°C compared to 50°C for direct heating, which degrades the HP COP.

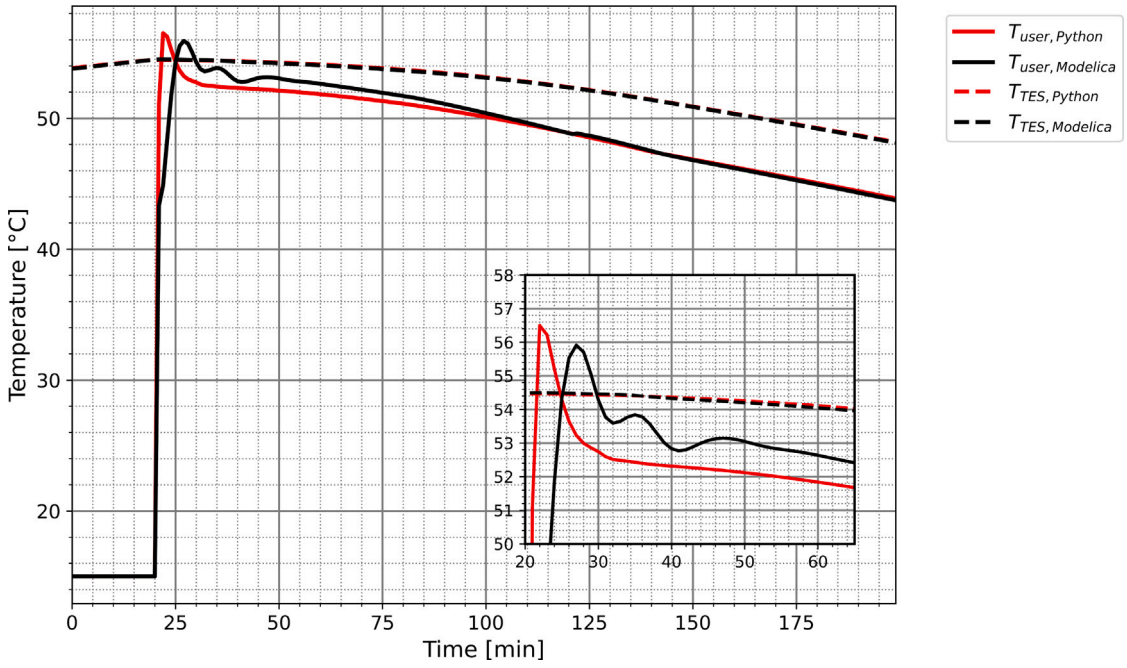


Fig. 11. Simulated temperature profiles at the upstream node of the thermal user (n_8) and the TES during discharging mode.

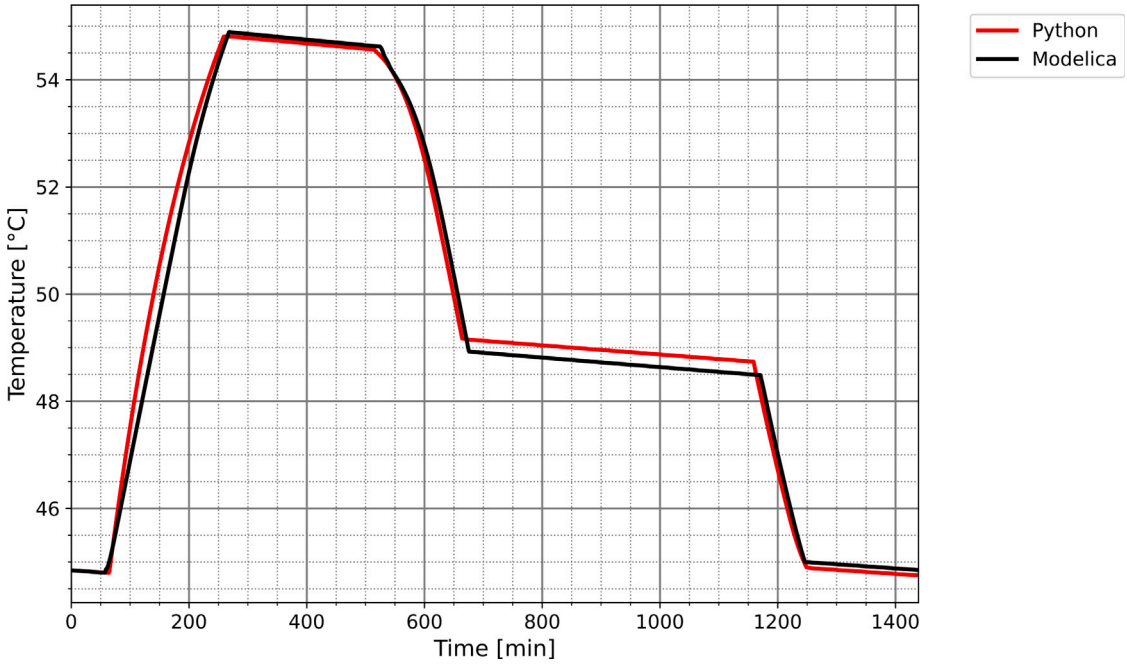


Fig. 12. Simulated temperature of the TES under an imposed operating routine consisting of charging, rest, and discharging phases.

Table 4
Main results in terms of energy, cost, and emissions for different operating schedules.

Scenario	E_{el} [kWh]	Cost [€]	Carbon emissions [kg_{CO_2}]
Direct heating (reference)	157.68	19.44	30.25
Cost minimization	174.23	18.47	31.96
Carbon minimization	176.09	19.95	30.66

However, from an economic perspective, using the TES proves to be an effective choice if properly controlled, as it reduces operating costs compared to the base case despite the higher energy consumption. Conversely, regarding emissions, using the TES results in a performance penalty, even with a dedicated operating schedule. Evidently, the variability of carbon intensity is not sufficient to offset the extra emissions generated by the additional energy consumed by the TES, making the base case the superior solution.

With reference to the chart describing the system electricity consumption across different scenarios (see Fig. 16), the cost minimization

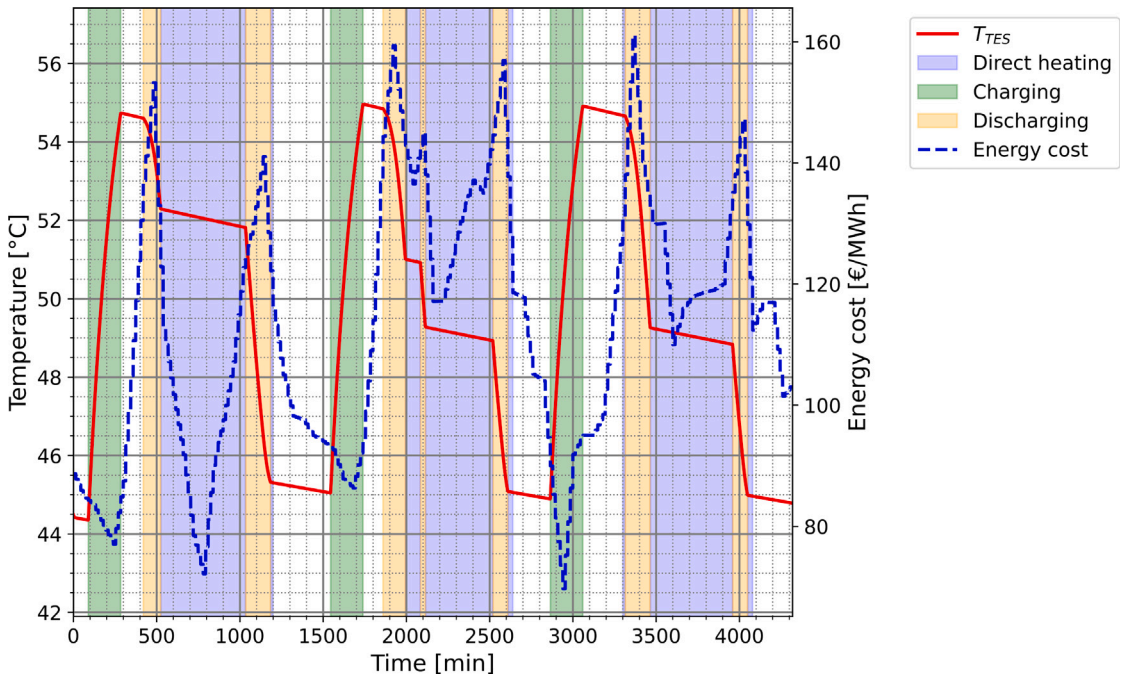


Fig. 13. TES temperature and energy cost profiles under a cost-minimized operating schedule.

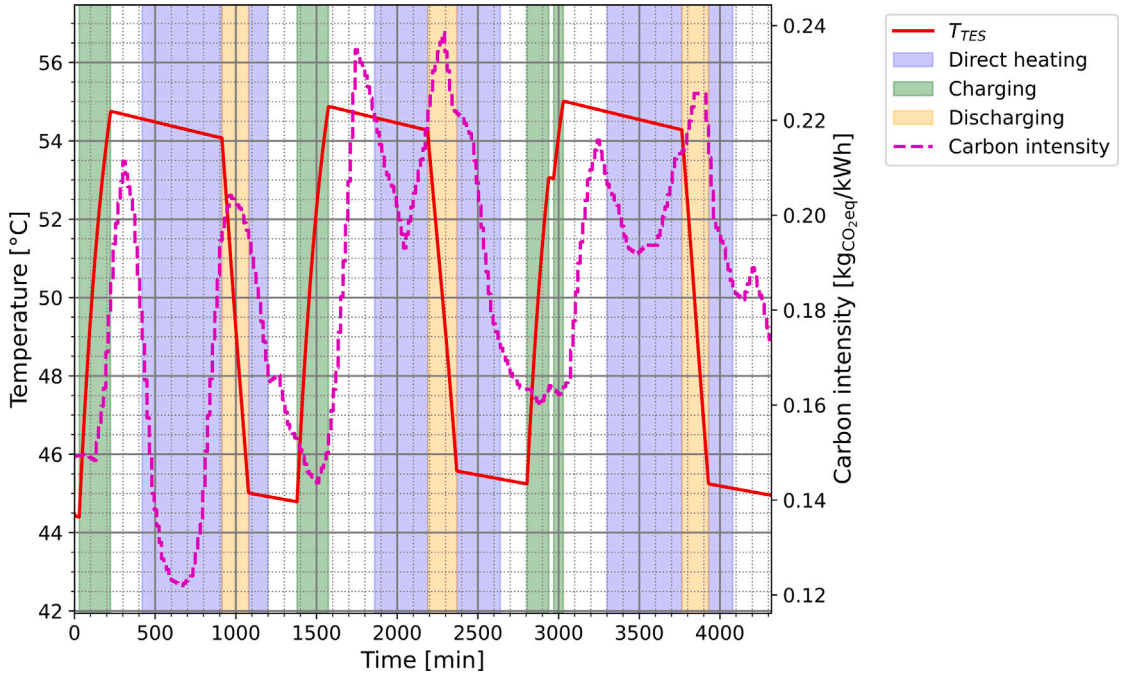


Fig. 14. TES temperature and carbon intensity profiles under a carbon-minimized operating schedule.

case is slightly more favorable than the emission minimization one. Since the storage units are the same size, the energy available during discharge remains constant, as does the user demand. Consequently, the total thermal energy supplied by the heat pumps is also the same.

However, because the TES discharge schedule differs between the due cases, the timing of heat pump activity and the required thermal capacity also change, while the total thermal energy over the entire period remains constant. Since the COP is a function of capacity, it varies between the two cases, creating the discrepancy in electricity consumption. Fig. 17 shows the HP COP profiles during the first day of simulation for both cases; values are omitted when the machines are off. Notably, between 400 and 1200 min, when the units are active in direct heating mode, they operate at different COPs, which accounts for the difference in absorbed electrical energy. Similar COP trends are observed during the other two days of simulation.

Table 5 reports the flexibility factor values calculated for each simulation scenario, in terms of both cost and carbon emissions. The results show that the direct heating scenario lacks flexibility for both emissions and cost, as the timing of energy consumption is strictly constrained by demand. In contrast, the cost and emission minimization scenarios

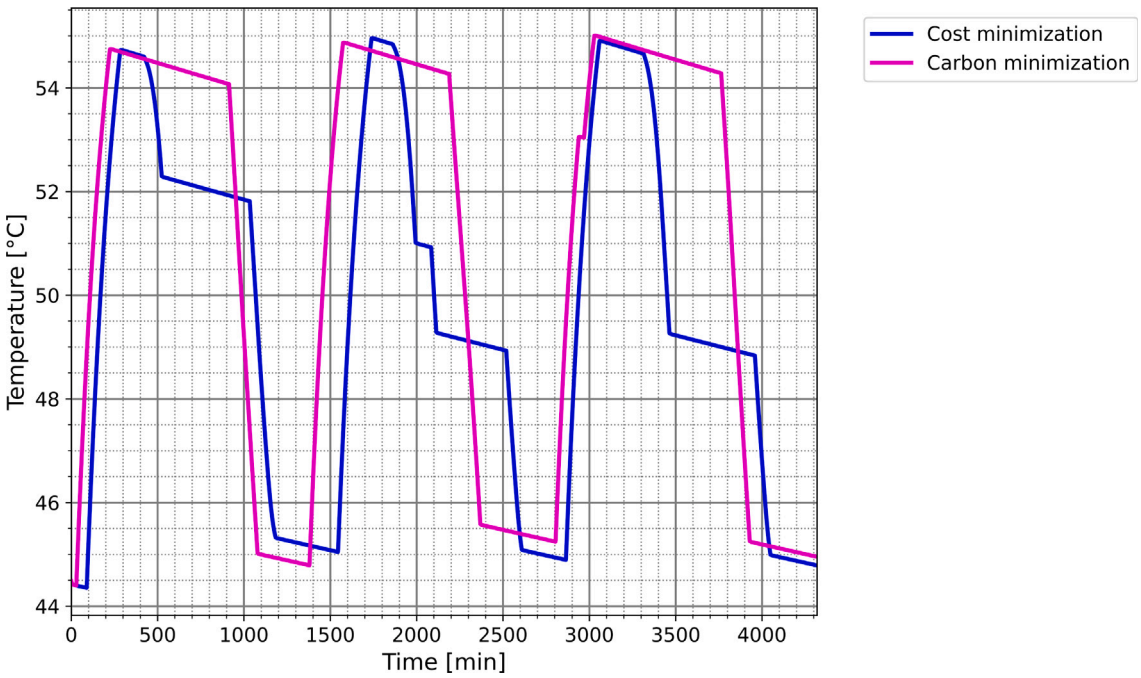


Fig. 15. TES temperature profiles under cost and carbon minimization operating schedules.

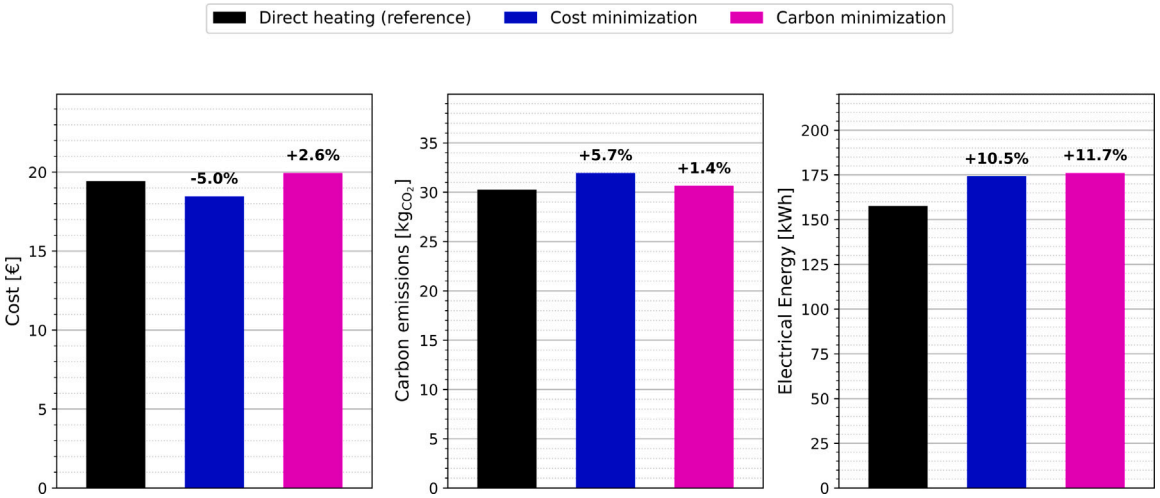


Fig. 16. Performance comparison of cost-minimized and carbon-minimized operating schedules against the direct heating reference in terms of energy, cost, and emissions.

Table 5
Flexibility factors for different operating schedules.

Scenario	Economic flexibility factor	Environmental flexibility factor
Direct heating (reference)	−0.58	−0.32
Cost minimization	**0.45**	0.06
Carbon minimization	−0.02	**0.50**

exhibit higher flexibility factors, demonstrating the system's ability to shift consumption toward periods of lower cost or environmental impact. This analysis reflects the trends shown in Fig. 16, illustrating the reduction in operating costs or emissions when the appropriate strategy is adopted. As previously observed, since the cost and carbon intensity curves are out of phase, minimizing cost does not yield optimal results for emissions, and vice versa.

5. Conclusions

This paper presents the development, validation and application of a numerical model for a flexible energy system, integrating water-to-water reversible heat pumps (WSHPs) with sensible Thermal Energy Storage (TES) systems. This work is part of a larger project aiming to convert this preliminary modeling framework into a full digital twin for the HPFlexLab experimental facility at the Politecnico di Torino.

The conclusions section discusses the two main categories of results obtained and the future developments of this work.

5.1. Model validation

Regarding model validation, the error metrics for the TES temperature remain remarkably low across both simulated scenarios (pure discharging and the complete charge/discharge routine). The RMSE does not exceed 0.3°C, while the maximum MAE is 0.22°C. The MBE

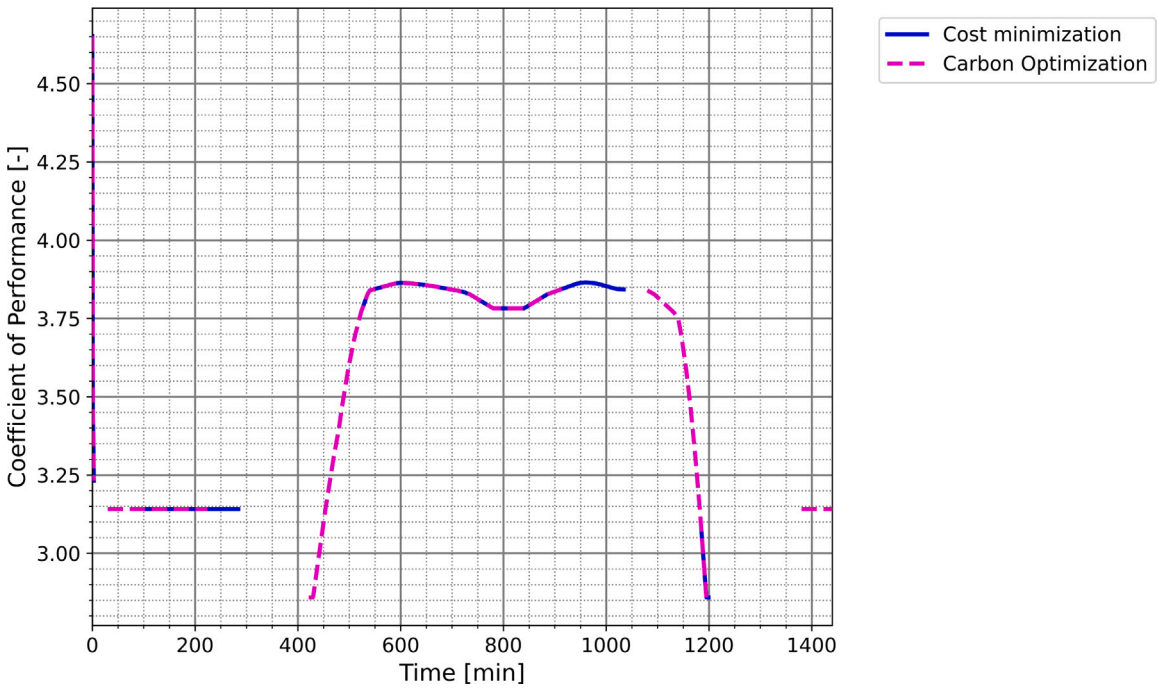


Fig. 17. HP COP profiles during the first day of simulation under cost and carbon minimization operating schedules.

is also minimal, reaching a maximum of 0.09°C; its slightly positive value in both cases indicates a minor tendency of the Python model to overestimate the temperature compared to Modelica.

In contrast, the temperature upstream of the load shows more pronounced differences. During direct heating, while the MAE and MBE remain low, the RMSE reaches a maximum of 2.19°C. This discrepancy is justified by the different control implementations on the heat pump. Modelica utilizes a PI controller, whereas Python instantaneously imposes the target temperature, which is a less realistic behavior. For the discharging phase, the MAE and MBE are again low, while the RMSE reaches 1.29°C. Although this difference cannot be attributed to a single specific factor, Fig. 11 shows that the two temperature profiles diverge only during the initial stages of the discharge process and align closely afterward. This suggests that the discrepancy stems from transient factors related to the operational mode switch of the plant. Furthermore, because the MBE for the temperature upstream of the load changes sign between the two cases, it is impossible to conclude whether the Python model systematically overestimates or underestimates that specific temperature.

5.2. Computational performance

In terms of computational cost, the Python model proves to be significantly more efficient. In the shorter direct heating and discharging simulations, Python requires approximately one third of the simulation time of Modelica. This performance gap widens drastically during the full charge/discharge routine, where the simulation time ratio reaches 9 to 1 in favor of Python.

Interestingly, the ratio between computation time and simulated time remains nearly constant for the Python model. It decreases slightly as the simulated period lengthens because the circuit characteristics are computed only once at the beginning of the simulation, acting as a fixed overhead.

Conversely, for the Modelica model, this ratio behaves differently. It remains roughly equal between the direct heating and discharging scenarios (at about 0.62 s per simulated minute), even though the direct heating simulation covers a period five times longer than the discharging one. However, during the full charge/discharge routine, this ratio doubles. This demonstrates that modeling the TES heat transfer across multiple operational modes (charging, rest, and discharging) requires substantial computational effort from Modelica.

Consequently, for multi-day simulations involving alternating TES charging and discharging phases, which represents the typical application of this type of model, the Python model is far preferable, especially considering its high fidelity in replicating the TES temperature profile.

5.3. Energy simulations

The analyzed case study compares different plant control scenarios by evaluating energy consumption, operational costs, carbon emissions, and the flexibility factor.

Regarding cost minimization, the system equipped with thermal storage and managed by the proposed control strategy successfully reduces operational costs by 5.0% compared to the baseline scenario. However, this savings comes at the expense of a 10.5% increase in energy consumption and a 5.7% increase in carbon emissions, highlighting that this economic advantage carries a considerable environmental impact. Conversely, when the control strategy aims to minimize emissions, the storage-equipped system proves unable to reduce the environmental impact compared to the baseline case, as shown in Fig. 16. Although this outcome is undoubtedly influenced by the specific emissions profile of the three simulated days, it remains highly significant.

Within the scope of this case study, it can be concluded that if a thermal storage unit is adopted, the environmental impact and energy consumption will consistently be higher than in the reference case without storage, regardless of the control strategy applied.

5.4. Limitations and future developments

In terms of plant modeling, the main improvements involve implementing more sophisticated models for the thermal load and the heat pump. While the current heat pump and external load models are simplified because the experimental facility is currently under construction and sufficiently accurate data for detailed dynamic modeling are not yet available, they have been temporarily modeled using this

simplified approach. Future developments should fully describe their transient behavior, leveraging the capability of the method used to model the entire hydraulic network. Furthermore, the model requires experimental validation in addition to the numerical one.

Instead, regarding the analysis of the case study, this is simplified by factors such as a thermal load that repeats identically every day and thermal energy storage control strategies that are overly refined, as they rely on input data that would normally be unavailable when controlling the plant in real time. Therefore, specifically from a real time control perspective and keeping in mind that this work is intended as a preliminary modeling framework for digital twin applications, it becomes necessary to make both the thermal load and the plant control more realistic. This can be achieved by utilizing estimates for the load profile, energy costs, and carbon intensity for the following day, combined with appropriate optimization algorithms.

Finally, regarding scalability and applicability to other HVAC systems, the framework is designed to easily adapt to different hydraulic or ventilation network topologies simply by updating the network layout in the input. If different components are present, introducing specific models to describe their behavior is sufficient for their integration into the overall system. Furthermore, since the numerical algorithm is tailored for district heating networks, the size of the system in terms of branches and nodes does not pose significant challenges during the modeling and resolution phases.

CRediT authorship contribution statement

Lorenzo Pellizzon: Data curation, Formal analysis, Investigation, Methodology, Software, Visualization, Writing – original draft, Writing – review & editing. **Matteo Bilardo:** Conceptualization, Investigation, Methodology, Supervision, Validation. **Enrico Fabrizio:** Conceptualization, Formal analysis, Funding acquisition, Project administration, Resources, Supervision, Validation. **Marco Perino:** Conceptualization, Formal analysis, Funding acquisition, Investigation, Project administration, Resources, Supervision.

Declaration of competing interest

The authors declare the following financial interests/personal relationships which may be considered as potential competing interests: Lorenzo Pellizzon reports financial support was provided by Ministero dell'Università e della Ricerca. Matteo Bilardo reports financial support was provided by Ministero dell'Università e della Ricerca. If there are other authors, they declare that they have no known competing financial interests or personal relationships that could have appeared to influence the work reported in this paper.

Acknowledgments

The authors carried out this study within the "Network 4 Energy Sustainable Transition – NEST", Project code PE0000021, Concession Decree No. 1561 of 11.10.2022 adopted by Ministero dell'Universitá e della Ricerca (MUR), CUP E13C22001890001. Project funded under the National Recovery and Resilience Plan (NRRP), Mission 4 Component 2 Investment 1.3 - Call for tender No. 341 of 15.03.2022 of MUR; funded by the European Union – NextGenerationEU.

Appendix

This appendix presents the mathematical derivation of the constitutive equations for two components of the modeled system, specifically the hydraulic network and the TES.

A.1. Constitutive equations and numerical formulation of the hydraulic network

This section details the formulation of the fluid dynamic and thermal problems for network elements, namely nodes and branches. These element level equations are then combined based on the network topology to formulate the global fluid dynamic and thermal problems in a structured matrix form. Finally, the solution strategy for the fluid dynamic problem using the SIMPLE method is described.

A.1.1. The fluid dynamic problem

As regard the fluid dynamic problem, velocity and pressure in a flow system are governed by the continuity and the momentum equations which are:

$$\frac{\partial \rho}{\partial t} + \nabla \cdot \rho v = 0 \tag{A.1}$$

$$\rho \frac{D\rho}{Dt} = -\nabla p - \nabla \cdot \tau + F \tag{A.2}$$

where F is the momentum source term that also includes the gravity term ρg, τ is the viscous stress tensor, $v \equiv v(x_1, x_2, x_3, t)$ is the velocity vector and $p \equiv p(x_1, x_2, x_3, t)$ is the static pressure. The Eqs. (A.1) and (A.2) are expressed for the 3D case, but, for the one-dimensional model, along the direction x_1, they can be simplified in the following form:

$$\frac{\partial \rho}{\partial t} + \frac{\partial (\rho v_1)}{\partial x_1} = 0 \tag{A.3}$$

$$\rho \frac{\partial v_1}{\partial t} + \rho v_1 \frac{\partial v_1}{\partial x_1} = -\frac{\partial p}{\partial x_1} - F_{FRICT} + F_1 \tag{A.4}$$

The mathematical formulation of τ involves partial derivatives with respect to the directions orthogonal to x_1, which have been neglected, which means that the viscous stress tensor τ loses significance in the case of a one-dimensional formulation. So in order to take viscous forces into account, the term $(\nabla \cdot \tau)_1$, which represents the net force due to viscous stress acting along the direction x_1, is replaced by F_{FRICT}, which is formulated on the basis of semi-empirical correlations.

The momentum source term F_1 considers the effects of pumps pressure rises and local fluid dynamic resistance due to valves or junctions in addition to the gravitational term, and so it can be expressed as:

$$F_1 = \rho g_{x_1} - F_{LOCAL} + F_{PUMP} \tag{A.5}$$

In the context of a one-dimensional model, it is useful to derive the integral form of the momentum equation (A.4) for a duct. This is done by integrating the equation over the control volume CV_1 (see Fig. A.1) which includes a portion of pipe between the inlet and outlet cross sections, as shown in Fig. A.1. The integration of Eq. (A.4) over CV_1 gives:

$$\int_{CV_1} \rho \frac{\partial v_1}{\partial t}\, dV + \int_{CV_1} \rho v_1 \frac{\partial v_1}{\partial x_1}\, dV + = \int_{CV_1} -\frac{\partial p}{\partial x_1}\, dV - \int_{CV_1} F_{FRICT}\, dV + \int_{CV_1} F_{x_1}\, dV \tag{A.6}$$

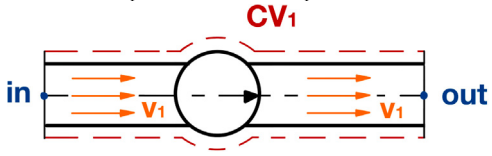


Fig. A.1. Control volume of a branch (CV_1).

The control volume CV_1 corresponds to the volume of the pipe, so $dV = S, dx_1$, where S is its cross-sectional area. This means that the volume integral can be expressed as an integral along the pipe length, from the inlet to the outlet. Based on this consideration, Eq. (A.6) can be reformulated in the following way:

$$\rho \frac{dv_1}{dt} SL + \rho \left[\frac{\left(v_{1,out}\right)^2 - \left(v_{1,in}\right)^2}{2} \right] S = \left(p_{in} - p_{out}\right) S - \rho g \left(z_{out} - z_{in}\right) S +$$

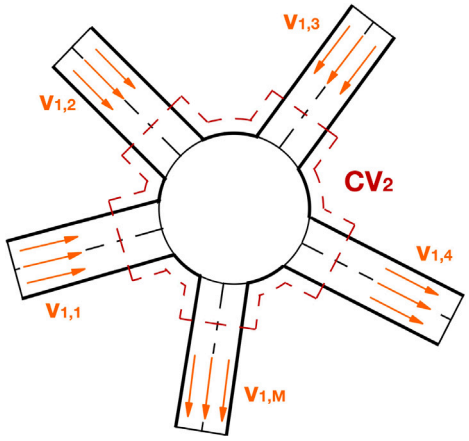


Fig. A.2. Control volume of a node (CV_2).

$$-\Delta P_{FRICT}S - \Delta P_{LOCAL}S + \Delta P_{PUMP}S \tag{A.7}$$

where L is the pipe length. The total pressure P is defined as

$$P \doteq p + \rho\frac{v^2}{2} + \rho g z \tag{A.8}$$

and the distributed and localized pressure losses can be expressed as

$$\Delta P_{FRICT} = \frac{1}{2} f \frac{L}{D_h}\rho(v_1)^2 \tag{A.9}$$

$$\Delta P_{LOCAL} = \frac{1}{2}\sum_k \beta_k \rho(v_1)^2 \tag{A.10}$$

where f and D_h are the friction factor and hydraulic diameter of the pipe, respectively, and β_k is a local loss coefficient related to the kth local loss occurring in the pipe.

Replacing the expressions (A.8), (A.9) and (A.10) in Eq. (A.7), it momentum equation can be expressed as follows

$$\rho\frac{dv_1}{dt}L + \left(P_{out} - P_{in}\right) = -\frac{1}{2} f \frac{L}{D_h}\rho(v_1)^2 - \frac{1}{2}\sum_k \beta_k \rho(v_1)^2 + \Delta P_{PUMP}S \tag{A.11}$$

After applying the momentum equation on the pipe, the attention goes to the junction that connects the pipes. Here a mixing or separation between different streams take place and the mass conservation in the junction can be expressed by integrating the continuity Eq. (A.3) over the control volume CV_2 (see Fig. A.2) which results in

$$\int_{CV_2}\frac{\partial \rho}{\partial t}\,dV + \int_{CV_2}\frac{\partial(\rho v_1)}{\partial x_1}\,dV = 0 \tag{A.12}$$

Applying the divergence theorem and solving the integrals, the following expression is obtained

$$\frac{d}{dt}M + \sum_{j=1}^{NB}\rho_j v_{1,j} S_j = 0 \tag{A.13}$$

where M refers to the mass of fluid in CV_2, S_j is the cross-section of the jth pipe connected to the junction and NB is the total number of branches connected to the node enclosed in CV_2. Further, it is possible to add a term in Eq. (A.12) to account for a possible injection or extraction of fluid from a junction to the external environment as

$$\frac{d}{dt}M + \sum_{j=1}^{NB}\rho_j v_{1,j} S_j + G_{ext} = 0 \tag{A.14}$$

A positive G_{ext} means extraction of fluid form the junction, while a negative value means injection into it.

A.1.2. The thermal problem

Dealing with a heating system requires to consider the heat transfer in the analysis. Since the circulating fluid is water, the compressibility effects and the viscous heating are negligible, allowing to apply the following expression of the energy equation:

$$\rho c_p\frac{\partial T}{\partial t} + \rho c_p v\cdot\nabla T = \nabla\cdot k\nabla T + \varphi_s \tag{A.15}$$

where k is the fluid thermal conductivity (assumed constant), c_p is the fluid specific heat capacity and $T \equiv T(x_1, x_2, x_3, t)$ is the temperature. As for the fluid dynamic problem, assuming one-dimensional flow, Eq. (A.15) can be simplified and expressed as

$$\frac{\partial\left(\rho c_p T\right)}{\partial t} + \frac{\partial\left(\rho c_p v_1 T\right)}{\partial x_1} = k\frac{\partial^2 T}{\partial x_1^2} + \varphi_s \tag{A.16}$$

where the volumetric heat source can be split into two terms:

$$\varphi_s = \varphi_v - \varphi_l \tag{A.17}$$

φ_v represents the heat generated within the system, while φ_l accounts for the effect of heat exchange at the walls, which would not be represented anyway because the corresponding temperature gradient is orthogonal to the x_1 direction and thus not modeled here.

As for the fluid dynamic problem, it is useful to integrate Eq. (A.16) over a proper control volume CV_3, which includes the junction node and half of each pipe entering or exiting the junction, as depicted in Fig. A.3. Adiabatic and perfect mixing is assumed and all the flows exiting from the junction are at the same temperature T. Then the following equation is obtained:

$$\begin{aligned}&\int_{CV_3}\frac{\partial\left(\rho c_p T\right)}{\partial t}\,dV + \int_{CV_3}\frac{\partial\left(\rho c_p v_1 T\right)}{\partial x_1}\,dV + \\ &= \int_{CV_3} k\frac{\partial^2 T}{\partial x_1^2}\,dV + \int_{CV_3}\varphi_v\,dV - \int_{CV_3}\varphi_l\,dV\end{aligned} \tag{A.18}$$

Applying the divergence theorem and solving the integrals, the above equation leads to the energy equation for a junction:

$$\underbrace{\frac{\partial(\rho c_p T)}{\partial t}\Delta V}_{\text{I}} + \underbrace{\sum_{j=1}^{NB}\rho_j c_{p,j} v_{1,j} T_j S_j}_{\text{II}} = \underbrace{\sum_{j=1}^{NB}\frac{\partial T}{\partial x_1}\bigg|_{S_j}}_{\text{III}} + \underbrace{\Phi_{v,i}}_{\text{IV}} - \underbrace{\Phi_{l,i}}_{\text{V}} \tag{A.19}$$

The term I refers to the rate of change of energy within CV_3 whose volume is ΔV and which is evaluated using the fluid temperature T at the junction. The term II refers to the net rate of energy transfer resulting from the mass flow rate entering and exiting the junction. The temperatures T_j are taken at the boundary of the control volume, which is something to define since the temperatures are only defined at the ends of each pipe (called nodes). The term III represents the net rate of energy transfer due to heat conduction, which is normally negligible in convection dominated problems (as this one). Finally, the terms IV and V derive from the volumetric source term (A.17) and are formulated using semi-empirical correlations. In particular, the term accounting for the heat losses $\Phi_{l,i}$ can be expressed as

$$\Phi_{l,i} = \sum_{j=1}^{NB}\frac{Lj}{2}\Omega_j U_j (T_i - T_\infty) \tag{A.20}$$

being Ω_j the perimeter of the jth branch, U_j the global heat transfer coefficient, T_i the node temperature and T_∞ the external temperature.

A.1.3. Graph-based network formulation of governing equations

In the one-dimensional approach adopted for this application, the structure of the heating system is modeled as a network of pipes connected through junctions and is described using graph theory [25]. A graph represents a set of interconnected objects, where each connection links a pair of objects (called *nodes*), although each object can be connected to multiple others through several links (called *branches*).

In the context of a heating network, *nodes* typically correspond to junctions, while *branches* represent components like pipes, ducts, channels, and similar elements that are bounded by two nodes.

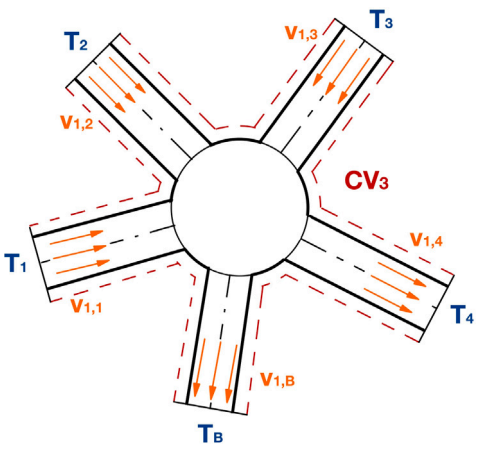


Fig. A.3. Control volume of a node (CV_3).

A fluid network is described through the interconnections between nodes and branches. These interconnections define the network topology and are represented by the *incidence matrix* A, which has one row for each node and one column for each branch. A generic element A_{ij} of this matrix is defined as follows:

- $A_{ij} = 1$ if the ith node is the *inlet* of the jth branch;
- $A_{ij} = -1$ if it is the *outlet*;
- $A_{ij} = 0$ if the node and branch are not directly connected.

Previously, the continuity Eq. (A.14) and the momentum equation (A.11) have been derived for, respectively, a single branch and a single node. Dealing with a network requires to apply those equations to all the nodes and branches of system, which can be easily done using the incidence matrix A.

As regard the continuity equation, assuming steady-state conditions, Eq. (A.14) can be formulated in matrix form for all the nodes of the network:

$$A \cdot G + G_{ext} = 0 \tag{A.21}$$

where G is a column vector containing the mass flow rates in the branches, and G_{ext} is the vector of mass flow rates injected into or extracted from the nodes by the external environment.

As done in the case of continuity, the momentum equation (A.11) can be extended to the whole network using the matrix formulation. In case of steady-state conditions, the equation becomes:

$$A^T \cdot P = R \cdot G - t, \tag{A.22}$$

where A^T is the transpose of the incidence matrix, P is a vector containing the total pressures at the nodes, G is the vector containing the mass flow rates in the branches, t is the vector of pressure increases due to pumps, and R is a diagonal matrix defined by

$$R_j = \frac{1}{2}\frac{G_j}{\rho S_j^2}\left(\frac{f_j}{L_j}D_j + \sum_k \beta_{k,j}\right) \tag{A.23}$$

Isolating G, one obtains:

$$G = Y \cdot A^T \cdot P + Y \cdot t, \tag{A.24}$$

with $Y = R^{-1}$ representing the fluid dynamic conductance. Proper boundary conditions must be applied to Eq. (A.24): typically the pressure is specified at the node corresponding to the pressurization system (downstream of the pump). Moreover, the mass flow rate boundary conditions for flows entering or exiting the network must be imposed on G_{ext}.

The same procedure for extending the equation to the entire network must also be carried out for the energy Eq. (A.19); neglecting conduction and remembering that $G = \rho v S$, it can be reformulated as:

$$\frac{d(\rho c_p T_i)}{dt}\sum_{j=1}^{NB}\frac{S_j L j}{2} + \sum_{j=1}^{NB} c_{p,j} G_j T_j = \Phi_{v,i} - \sum_{j=1}^{NB}\frac{Lj}{2}\Omega_j U_j (T_i - T_\infty) \tag{A.25}$$

Note that the energy equation must be expressed in transient form because thermal perturbations propagate much slower than pressure waves. While flow variations are rapidly transmitted as pressure waves (typically in tenths of a second), temperature changes travel at water velocity (around 1 m/s in a heating system) and may reach end-users after several minutes, especially over long distances. For this reason, the model employs a quasi-dynamic approach: flow and pressure are obtained via static analysis, whereas temperature is dynamically evaluated.

Furthermore, as shown in Eq. (A.25), it is necessary to define the temperature T_j at each control volume boundary (i.e., at the midpoint of each branch) as a function of the nodal temperatures T_i, which are the unknowns of the problem. Once this relation is established, the equations can be formulated in matrix form. For a convective dominated problem, as this one, the most suitable numerical scheme is the upwind differencing scheme, which takes into account the flow direction of the stream. Using this method, the temperature value at a cell face is taken equal to the one of the upstream node.

The last aspect to define in Eq. (A.25) is the time discretization, which can be done using the backward Euler method, obtaining the following expression:

$$\frac{\left(\rho_i c_{p,i} T_i\right)^t - \left(\rho_i c_{p,i} T_i\right)^{t-\Delta t}}{\Delta t}\sum_{j=1}^{NB}\frac{S_j L j}{2} + \sum_{j=1}^{NB} c_{p,j} G_j^t T_j^t$$

$$= \Phi_{v,i}^t - \sum_{j=1}^{NB}\frac{Lj}{2}\Omega_j U_j (T_i^t - T_\infty) \tag{A.26}$$

Finally, extending Eq. (A.26) for each node of the network, the complete set of energy equations can be written in matrix form:

$$\left(M^t + K^t\right)\cdot T^t = f^t + \Phi_{v,i}^t + M^{t-\Delta t}\cdot T^{t-\Delta t} \tag{A.27}$$

where M is the mass matrix (diagonal), whose entries are related to the time-dependent term of Eq. (A.26), K is the stiffness matrix whose entries are related to the convective term and to those terms of the heat losses depending on T_i, f is a vector containing the known term related to the heat source $\Phi_{v,i}$ and those terms of the heat losses depending on T_∞. Finally, T is the vector containing the temperatures at each node of the network.

The boundary conditions need to be defined when solving Eq. (A.26), and typically this is done by imposing the temperature at the appropriate nodes of the network.

A.1.4. The Semi-Implicit Method for Pressure-Linked Equations (SIMPLE) algorithm

Since the matrix Y itself depends on the mass flow rates, the resulting system of equations is nonlinear. Moreover, the strong coupling between the mass (A.21) and momentum (A.22) equations requires an iterative solution method. According to [26], the SIMPLE (Semi-Implicit Method for Pressure-Linked Equations) algorithm [24] can be efficiently applied. This algorithm uses a guess-and-correction approach. First, a pressure vector P' and a mass flow rate vector G_0' are guessed, thereby allowing the construction of Y'. Then, Y' is used to compute the new value of G' as:

$$G' = Y' \cdot A^T \cdot P' + Y' \cdot t \tag{A.28}$$

where the solution of (A.28) is obtained with a fixed-point algorithm [35]. Since the guessed pressure and mass flow rates differ from the correct values, corrections are introduced:

$$P = P' + P_{corr} \tag{A.29}$$

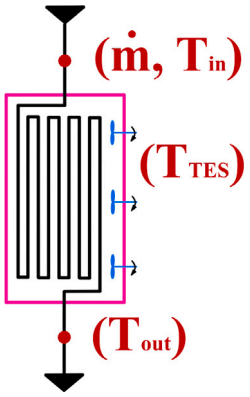


Fig. A.4. Scheme of the TES model.

$$G = G' + G_{corr} \tag{A.30}$$

and, by combining (A.22) and (A.28), one obtains

$$G - G' = Y \cdot A^T \cdot P - Y' \cdot A^T \cdot P' + (Y - Y') \cdot t \tag{A.31}$$

Assuming $Y' = Y$ and substituting (A.29) and (A.30) into (A.31), the mass flow rate correction is given by

$$G_{corr} = Y \cdot A^T \cdot P_{corr} \tag{A.32}$$

Substituting (A.30) and (A.32) into the mass conservation Eq. (A.21) yields

$$A \cdot Y' \cdot A^T \cdot P_{corr} = -A \cdot G' - G_{ext} \tag{A.33}$$

Defining $H = A \cdot Y' \cdot A^T$ and $d = -A \cdot G' - G_{ext}$, Eq. (A.33) can be rewritten in a compact form as

$$H \cdot P_{corr} = d \tag{A.34}$$

Once P_{corr} is computed from (A.34), G_{corr} is obtained from (A.32), and the updated values P and G are given by (A.29) and (A.30), respectively. To improve convergence, under-relaxation factors are applied so that (A.29) and (A.30) become

$$P = P' + \alpha P_{corr} \tag{A.35}$$

$$G = G' + \alpha G_{corr} \tag{A.36}$$

with α being the under-relaxation factor. Finally, appropriate boundary conditions must be enforced: the mass flow rates at the network boundaries (imposed on G_{ext}) and the pressure in at least one node of P' are prescribed exactly.

Once the pressures and flow rates are computed, respectively, in all the nodes and branches of the network, the mass matrix M, the stiffness matrix K and the known term f can be assembled and the temporal evolution of the nodes temperature can be calculated solving Eq. (A.27).

A.2. Thermal energy storage constitutive equations

The mathematical formulation of the storage component is based on transient energy balance equations. The physical system and the thermal interactions between the fluid domains are schematically shown in Fig. A.4.

The governing equations are structured to evaluate the temperature evolution within the system. Specifically, Eq. (A.37) defines the average fluid temperature within the serpentine coil. Eq. (A.38) describes the transient energy balance of the storage tank, which is used to calculate the tank fluid temperature T_{TES}. Finally, Eq. (A.39) governs the thermal behavior of the fluid within the serpentine, allowing the calculation of its outlet temperature T_{out}.

Note that T_{out} depends on the flow direction, which changes during the charging and discharging phases. Furthermore, the convective heat transfer coefficients are evaluated through fluid dynamic correlations [36] that account for the local velocity variations induced by the system stirrers.

$$T = \frac{T_{out} + T_{in}}{2} \tag{A.37}$$

$$M_{TES} C_p \frac{dT_{TES}}{dt} = U A (T - T_{TES}) - U_{TES} A_{TES} (T_{TES} - T_\infty) \tag{A.38}$$

$$\frac{M C_p}{2} \frac{dT_{out}}{dt} = \dot{m} C_p (T_{in} - T_{out}) - U A (T - T_{TES}) \tag{A.39}$$

Data availability

Data will be made available on request.

References

[1] European Commission, A clean planet for all: A European strategic long-term vision for a prosperous, modern, competitive and climate neutral economy, 2018, URL https://eur-lex.europa.eu/legal-content/EN/TXT/?uri=CELEX:52018DC0773.
[2] Fabrizio Ascione, Sandro Nižetić, Fuqiang Wang, Future technologies for building sector to accelerate energy transition, Energy Build. 326 (2025) 115044.
[3] Minjin Kong, Changyoon Ji, Taehoon Hong, Hyuna Kang, Impact of the use of recycled materials on the energy conservation and energy transition of buildings using life cycle assessment: a case study in South Korea, Renew. Sustain. Energy Rev. 155 (2022) 111891.
[4] International Energy Agency (IEA), Heating, 2022, URL https://www.iea.org/reports/heating.
[5] Khalid Ghazwani, Thomas Beach, Yacine Rezgui, Energy retrofitting using advanced building envelope materials for sustainable housing: A review, Build. Environ. 267 (2025) 112243.
[6] Rajan Kumar Jaysawal, Suprava Chakraborty, D Elangovan, Sanjeevikumar Padmanaban, Concept of net zero energy buildings (NZEB)-A literature review, Clean. Eng. Technol. 11 (2022) 100582.
[7] Francesco Asdrubali, Ilaria Ballarini, Vincenzo Corrado, Luca Evangelisti, Gianluca Grazieschi, Claudia Guattari, Energy and environmental payback times for an NZEB retrofit, Build. Environ. 147 (2019) 461–472.
[8] European Commission, Energy performance of buildings directive (EPBD), 2024, URL https://energy.ec.europa.eu/topics/energy-efficiency/energy-efficient-buildings/energy-performance-buildings-directive_en.
[9] İzzet Yüksek, İlker Karadağ, İ Yüksek, İ Karadağ, Use of renewable energy in buildings, Renew. Energy-Technol. Appl. 23 (2021).
[10] Matthew D. Leonard, Efstathios E. Michaelides, Grid-independent residential buildings with renewable energy sources, Energy 148 (2018) 448–460.
[11] Behnaz Rezaie, Ebrahim Esmailzadeh, Ibrahim Dincer, Renewable energy options for buildings: Case studies, Energy Build. 43 (1) (2011) 56–65.
[12] Thibault Q. Péan, Jaume Salom, Ramon Costa-Castelló, Review of control strategies for improving the energy flexibility provided by heat pump systems in buildings, J. Process Control 74 (2019) 35–49.
[13] Maarten Evens, Alice Mugnini, Alessia Arteconi, Design energy flexibility characterisation of a heat pump and thermal energy storage in a comfort and climate box, Appl. Therm. Eng. 216 (2022) 119154.
[14] José Sánchez Ramos, Mcarmen Pavón Moreno, Mcarmen Guerrero Delgado, Servando Álvarez Domínguez, Luisa F Cabeza, Potential of energy flexible buildings: Evaluation of DSM strategies using building thermal mass, Energy Build. 203 (2019) 109442.
[15] Monika Hall, Achim Geissler, Load control by demand side management to support grid stability in building clusters, Energies 13 (19) (2020) 5112.
[16] Qingrong Liu, Yongchun Liu, Fanyue Qian, Tingting Xu, Hua Meng, Yuting Yao, Yingjun Ruan, Demand response in buildings: Comparative study on energy flexibility potential of underfloor heating and air conditioning systems, Appl. Therm. Eng. (2025) 126801.
[17] Alessia Arteconi, Neil J. Hewitt, Fabio Polonara, Domestic demand-side management (DSM): Role of heat pumps and thermal energy storage (TES) systems, Appl. Therm. Eng. 51 (1–2) (2013) 155–165.
[18] Abdul Afram, Farrokh Janabi-Sharifi, Review of modeling methods for HVAC systems, Appl. Therm. Eng. 67 (1–2) (2014) 507–519.

[19] Xing Wang, Tao Li, Yingying Yu, Qingxia Liu, Lei Shi, Jingtao Xia, Qianjun Mao, Performance simulation and energy efficiency analysis of multi-energy complementary HVAC system based on TRNSYS, Appl. Therm. Eng. 257 (2024) 124378.
[20] Gianluca Coccia, Paola D'Agaro, Giovanni Cortella, Fabio Polonara, Alessia Arteconi, Demand side management analysis of a supermarket integrated HVAC, refrigeration and water loop heat pump system, Appl. Therm. Eng. 152 (2019) 543–550.
[21] Yurun Guo, Jihong Wang, Shugang Wang, Wenji Song, Zhenjun Ma, Shuang Jiang, Design and flexible operation study of a bidirectional thermal substation based on building thermal battery model in fifth generation heating and cooling systems, Appl. Therm. Eng. (2025) 128817.
[22] Guanyu Tian, Qun Zhou Sun, Wenyi Wang, Real-time flexibility quantification of a building HVAC system for peak demand reduction, IEEE Trans. Power Syst. 37 (5) (2021) 3862–3874.
[23] Marcus Vogt, Klemens Koch, Artem Turetskyy, Felipe Cerdas, Sebastian Thiede, Christoph Herrmann, Model-based energy analysis of a dry room HVAC system in battery cell production, Procedia CIRP 98 (2021) 157–162.
[24] S.V. Patankar, Numerical heat transfer and heat flow, series in computational methods in mechanics and thermal science, 1980.
[25] Harary F., Graph Theory, Narosa Publishing House, New Delhi, 1995.
[26] Elisa Guelpa, Adriano Sciacovelli, Vittorio Verda, Thermo-fluid dynamic model of large district heating networks for the analysis of primary energy savings, Energy 184 (2019) 34–44.
[27] Adriano Sciacovelli, Romano Borchiellini, Vittorio Verda, Numerical Design of Thermal Systems, Clut, 2015.
[28] Michael Wetter, Wangda Zuo, Thierry S Nouidui, Xiufeng Pang, Modelica buildings library, J. Build. Perform. Simul. 7 (4) (2014) 253–270.
[29] Francesco Witte, Ilja Tuschy, TESPy: Thermal engineering systems in python, J. Open Source Softw. 5 (49) (2020) 2178.
[30] Marco Perino, Matteo Bilardo, Enrico Fabrizio, Enhancing energy flexibility in buildings: A design-phase approach to couple latent heat thermal energy storage (LHTES) and heat pumps, in: Proceedings of the 16th IAE EST CP International Conference on Energy Storage, Lyon, France, 2024, URL https://www.polito.it/eng/research/tebe.
[31] Gestore dei Mercati Energetici (GME). https://www.mercatoelettrico.org.
[32] Electricity Maps. https://app.electricitymaps.com.
[33] Ilaria Vigna, Roberta Pernetti, Wilmer Pasut, Roberto Lollini, Literature Review on Energy Flexibility Definitions and Indicators for Building Clusters, Technical Report, International Energy Agency (IEA), Energy in Buildings and Communities Programme (EBC), 2018, URL https://www.annex67.org/media/1863/literature-review-on-energy-flexibility-definitions-and-indicators-for-building-clusters.pdf.
[34] Jérôme Le Dréau, Per Heiselberg, Energy flexibility of residential buildings using short term heat storage in the thermal mass, Energy 111 (2016) 991–1002.
[35] Alfio Quarteroni, Riccardo Sacco, Fausto Saleri, Numerical Mathematics, vol. 37, Springer Science & Business Media, 2010.
[36] Frank P Incropera, David P DeWitt, Theodore L Bergman, Adrienne S Lavine, et al., Fundamentals of Heat and Mass Transfer, vol. 6, Wiley, New York, 1996.